Eng. Sci., 2025, **36**, 1665

Engineered Science
DOI: https://dx.doi.org/10.30919/es1665

Construction of 0D Zinc Oxide Nanoparticles Anchored on the Surface of 2D MXene Functional Materials for High-efficiency Photocatalytic Removal of Organic Pollutants: Roles of Nanoconfinement Effect and Interface Effect

Chuanxi Yang,[1,#] Mingfang Zhang,[1,#] Yongkun Wu,[1] Kaipeng Sun,[1] Haowei Dang,[1] Yiyong Xu,[1] Jinran Zhang,[1] Chen Zhang,[1] Ruihong Chang,[1] Erling Zhao,[1] Yunlong Lan,[1] Haofen Sun,[1] Dong Chen,[1] Weihua Zhao,[1] Yihua Xiao,[1] Yizhen Tang,[1] Yuqi Fan,[2] Weiliang Wang,[1] Feng Dang[3,*] and Xiaoning Wang[1,*]

Abstract

Zinc oxide (ZnO) nanoparticles anchored onto the MXene surface (ZnO/MXene photocatalysts) were synthesized via hydrofluoric acid etching and solventthermal method. The photocatalytic performance of ZnO/MXene composites was evaluated by degrading methyl orange (MO) and p-nitrophenol (p-NP). MXene has a lamellar structure, while ZnO nanoparticles mostly form aggregated spheres. The ZnO/MXene composite maintains this lamellar morphology, with aggregated spherical ZnO nanoparticles on the surface, edges, and interlayer spaces of lamellar structure, thus forming a sandwich-like composite. When the mass ratio of ZnO to MXene in ZnO/MXene composite is 1:1 and catalyst dosage is 0.5 g·L-1 or 0.7 g·L-1, the optimal removal rates for MO and p-NP reach 100% and 74%, respectively. Compared to individual MXene and ZnO, the ZnO/MXene composite shows enhanced photocatalytic activity. This can be attributed to the nanoconfinement effect of MXene and interface interactions between ZnO and MXene. The change in surface charge distribution mainly stems from the S=O bond for MO, causing an increase in energy gap and chemical hardness of its degradation intermediates. However, the surface charge distribution changes are mainly due to the N=O bond for p-NP, resulting in increased the highest occupied molecular orbital (E_{HOMO}) values and chemical potential, while the electronegativity and Electrophilicity indices decrease in its degradation intermediates.

Keywords: ZnO/MXene; Interface effect; Nanoconfinement effect; Photocatalysis; Water treatment.
Received: 22 April 2025; Revised: 26 June 2025; Accepted: 27 August 2025.
Article type: Research article.

1. Introduction

Semiconductor-assisted photocatalysis plays a crucial role among various advanced oxidation methods in water treatment.[1] Among numerous semiconductors, the zinc oxide (ZnO) photocatalyst is extensively applied in the wastewater treatment field. This is because of its advantages such as easy preparation, low cost, environmental friendliness, stable properties, and good photocatalytic performance. However, ZnO has certain limitations in photocatalytic reactions. Its energy gap of 3.37 eV restricts it to absorbing only ultraviolet light.[2] Moreover, the photocatalytic activity of ZnO is also constrained by the low charge-separation efficiency caused by the recombination of electron-hole pairs.[3] These limitations are detrimental to the practical application of ZnO in environmental purification.[4] To achieve high reaction efficiency, the recombination of electrons and holes needs to be kept at a low level. Thus, it is essential to broaden the energy range of light excitation and improve the separation efficiency of hole-electron of ZnO. Therefore, the preparation of ZnO photocatalysts with high activity and excellent photostability is of great significance in water treatment. To

[1] *School of Environmental and Municipal Engineering, Qingdao University of Technology, Qingdao, 266520, China*
[2] *College of Geography and Environment, Shandong Normal University, Jinan, 250358, China*
[3] *Key Laboratory for Liquid-Solid Structural Evolution and Processing of Materials, Shandong University, Jinan, 250061, China*
[#] *These authors contributed to this work equally.*
**Email*: dangfeng@sdu.edu.cn (F. Dang); wangxiaoning@qut.edu.cn (X.N. Wang)

enhance the photocatalytic activity of ZnO photocatalysts, traditional methods such as doping, dye sensitization, and defect engineering have been employed.[5] Nevertheless, these modifications often fail to substantially boost the photocatalytic performance of ZnO. An alternative approach to improving the photocatalytic activity of ZnO is to fabricate 0D/2D photocatalysts in combination with MXene. Khadidja *et al*. reported the synthesis of ZnO nanoparticles anchored onto the MXene surface (ZnO/MXene photocatalysts) composites through a straightforward two-step chemical reaction. The results indicate that ZnO/MXene composites prepared at 90 °C exhibit superior photocatalytic activity compared to pure ZnO microparticles.[6] After 21 minutes of irradiation, the degradation rate of the ZnO/MXene composite reached 87.5%, while that of pure ZnO microparticles was only 71.2% after 80 minutes of irradiation.

The 2D material MXene, with a graphene-like structure, has an obvious hollow structure. Its conductive electrons are separated from hole-electron pairs, thereby improving the utilization efficiency of hole-electron pairs. Due to its two-dimensional structure, MXene has a large specific surface area, which enables it to effectively adsorb organic pollutants. Moreover, the limited space inside the material can effectively enhance the photocatalytic activity. Li *et al*. synthesized a Z-scheme photocatalyst, ZnO@Nb_2CT_x MXene@carbon nitride nanosheets (ZNC), through a hydrothermal method combined with an electrostatic self-assembly strategy.[7] Degradation tests showed that after 40 minutes of light exposure, the removal rate of enrofloxacin reached 98.2%, with a degradation rate of 0.0961 min^{-1}. This degradation rate is 4.78 times higher than that of pure ZnO and 3.987 times higher than that of carbon nitride nanosheets (CNNS). The introduction of the MXene electron-transport layer was the primary factor contributing to the enhanced degradation efficiency. This is because it promotes charge transfer and the separation of electron-hole pairs, probably due to the nanoconfinement effect of MXene. However, the mechanism by which MXene enhances photocatalytic efficiency remains unclear, hence, it is meaningful and significant to expose the photocatalytic enhanced mechanism for the design of highly efficient photocatalysis-based wastewater treatment system.

Some studies have shown that the combination of ZnO and MXene exhibits an interface effect, which can enhance the photocatalytic activity. Gong *et al*. used Cu-Co-Al layered double hydroxide (LDH) grafted onto sulfur-doped coffee biochar (SCB) Cu-Co-Al/SCB catalyst for selective synthesis of cyclopentanol (CPL) from biomass-derived furfural (FAL), the results indicated that Cu-Co-Al/SCB achieved a maximum CPL yield of 97.5% and a high turnover frequency (TOF) of 15.6 h^{-1} in the selective hydrogenative rearrangement of FAL at 140 °C, and the enhanced catalytic mechanism was grafting Cu-Co-Al onto SCB results in the formation of Cu-Co alloys and a strong interaction and the strong interaction between the Cu-Co alloy and sulfur-doped coffee biochar endowed Cu-Co-Al/SCB with remarkable stability.[8,9] Liu *et al*. prepared a novel diatomic Fe/Mo catalyst (Fe/Mo-DACs) to enhance the interfacial reaction mechanism with oxidant to achieve more stronger selective degradation of electron-donating organic pollutants, the results indicated that the degradation rate of bisphenol A (BPA) in Fe/Mo-DACs/PMS system (0.642 min^{-1}) was increased by two times compared with the corresponding Fe single-atomic reaction system, and the enhanced Fenton catalytic mechanism was the diatomic Fe/Mo site was the true activation center of PMS, and other independent single-atom Fe sites cooperated to optimize the interface reaction mechanism (adsorption and activation) of PMS on the materials' surface.[10] Hao *et al*. prepared a novel catalyst with unique $Ti_3C_2T_x$ MXene-regulated Ag-ZnO interfaces to use in electrocatalytic CO_2 reduction, the results indicated that the designed Ag-ZnO/$Ti_3C_2T_x$ catalyst achieves an outstanding CO_2 conversion performance of a nearly 100% CO Faraday efficiency with high partial current density of 22.59 mA cm^{-2} at -0.87 V versus reversible hydrogen electrode, and the enhanced electrocatalytic mechanism was the electronic donation of Ag and up-shifted d-band center relative to Fermi level within MXene-regulated Ag-ZnO interfaces contributes the high selectivity of CO, which enlightens the rational design of unique metal-oxide interfaces with the regulation of MXene for high-performance catalysis.[11] Therefore, it is necessary to construct the synergetic enhancement of 0D/2D ZnO/MXene based on the interface effect and nanoconfinement effect.

In this paper, ZnO/MXene photocatalysts were synthesized *via* the hydrofluoric acid (HF) etching and solventthermal method. The physicochemical properties of ZnO, MXene, and ZnO/MXene composites are characterized and analyzed using scanning electron microscopy (SEM)/energy-dispersive X-ray spectroscopy (EDS), X-ray diffraction (XRD), X-ray photoelectron spectroscopy (XPS), Fourier transform infrared spectroscopy (FTIR), Raman spectrum (Raman), ultraviolet-visible (UV-Vis) spectroscopy, and transmission electron microscope (TEM) techniques. Taking methyl orange (MO) and *p*-nitrophenol (*p*-NP) as the target pollutants, the catalytic degradation performance and mechanism of the ZnO/MXene composites towards MO and *p*-NP are investigated. The effects of the ratio of ZnO to MXene, the amount of the catalyst used, the pH value, and the initial concentration of the pollutants on the degradation of MO and *p*-NP by the composites are explored. Through kinetic fitting, toxicity calculation, degradation pathway analysis, electrostatic potential examination, and orbital variation rule studies, the degradation characteristics and molecular mechanism of the composites in the degradation of MO and *p*-NP are elucidated. The results can provide scientific and theoretical support for the design of efficient photocatalytic systems and their applications in water treatment.

2. Materials and methods

2.1 Materials and reagents

Zinc acetate ($Zn(AC)_2{\cdot}2H_2O$), sodium hydroxide (NaOH),

anhydrous ethanol (C_2H_6O), HF, MO ($C_{14}H_{14}N_3NaO_3SNa$), and *p*-NP ($C_6H_5NO_3$) were purchased from Sinopharm Group Chemical Reagent Co., Ltd. MAX (Ti_3AlC_2) was purchased from Shanghai Macklin Biochemical Technology Co., Ltd. All of these reagents were of AR grade and used without further purification. Deionized water was used to prepare all the solutions.

2.2 Preparation of photocatalysts

The preparations of the three materials are shown in Scheme 1.

Preparation of ZnO: Initially, 80 mL of absolute ethanol was added to a beaker to serve as the reaction solvent. Subsequently, 0.22 g of $Zn(AC)_2{\cdot}2H_2O$ and 0.064 g of NaOH were added to the ethanol and mixed thoroughly. The mixture was then placed on a temperature-controlled magnetic stirrer and magnetically stirred for 2 h at 80 °C. Following this, the mixture was directly transferred to a Teflon-lined autoclave, sealed, and reacted at 180 °C for 12 h. After the reaction was completed, the mixture was cooled to room temperature and washed by centrifugation with ethanol and deionized water for more than five times until it became neutral. The solid precipitate was then dried in an oven at 80 °C for 3 h. Finally, the sample was annealed in a muffle furnace at 400 °C for 2 h, cooled to room temperature, and ground to obtain ZnO nanoparticles.[12]

Preparation of MXene: First, 10 mL of a 40% HF solution was added to a beaker as the etching agent. Then, 1 g of Ti_3AlC_2 powder was slowly added because the reaction is vigorous. The mixture was magnetically stirred at 60 °C for 12 h. After the reaction, the suspension was poured out and centrifuged at 3500 rpm for 5 minutes. The pH of the supernatant was measured, and the supernatant was washed with deionized water to adjust the pH until it stabilized between 5 and 8. The product was further purified by centrifugally washing it twice with absolute ethanol and then vacuum-dried at 60 °C for 24 h to obtain Ti_3C_2 MXene.

Preparation of ZnO/MXene: ZnO/MXene composites with different mass ratios (MXene to ZnO ratios of 1:3, 1:2, 1:1, 2:1, and 3:1) were synthesized using a solvothermal method. Taking the composite photocatalyst with a MXene-to-ZnO mass ratio of 1:1 as an example, 80 mL of absolute ethanol was used as the solvent, and 0.2 g of MXene powder was added to it. The mixture was ultrasonicated for 20 minutes to ensure uniform dispersion. Next, 0.22 g of $Zn(AC)_2{\cdot}2H_2O$ and 0.064 g of NaOH were added to the solution, which was then stirred to mix well. The mixture was placed on a temperature-controlled magnetic stirrer and stirred at 80 °C for 2 h. It was subsequently transferred to a 100 mL Teflon-lined autoclave, sealed, and allowed to react at 180 °C for 12 h. After cooling to room temperature, the mixture was washed by centrifugation with deionized water and ethanol more than five times until it became neutral. The samples were dried in an oven at 80 °C for 3 h and then annealed in a muffle furnace at 400 °C for 2 h. After cooling, the ZnO/MXene composites were obtained by grinding.

2.3 Characterization of photocatalysts

The structure and morphology of the sample were characterized by SEM (Zeiss Gemini 300, Germany) and transmission electron microscopy (TEM, JEOL JEM - 2100F, Japan). The areal scanning analysis of Ti, C, O, and Zn elements was conducted by EDS of transmission electron microscopy. XRD patterns were recorded on a Bruker D8 Advance X-ray diffractometer with Cu Kα radiation (λ = 1.5418 A) and were used to determine the crystal structure and phase composition of the prepared photocatalysts. The FTIR spectra were collected on a Thermo Scientific Nicolet IS5 Fourier Transform infrared spectrometer (Waltham, MA, USA) in the wavenumber range of 400-4000 cm^{-1} with a resolution appropriate for the KBr pellet method and were used to characterize the functional groups of the photocatalyst. Raman spectrum was obtained using a confocal Raman microscope Horiba LabRAM HR (Horiba, Billerica, MA, USA) with a 10

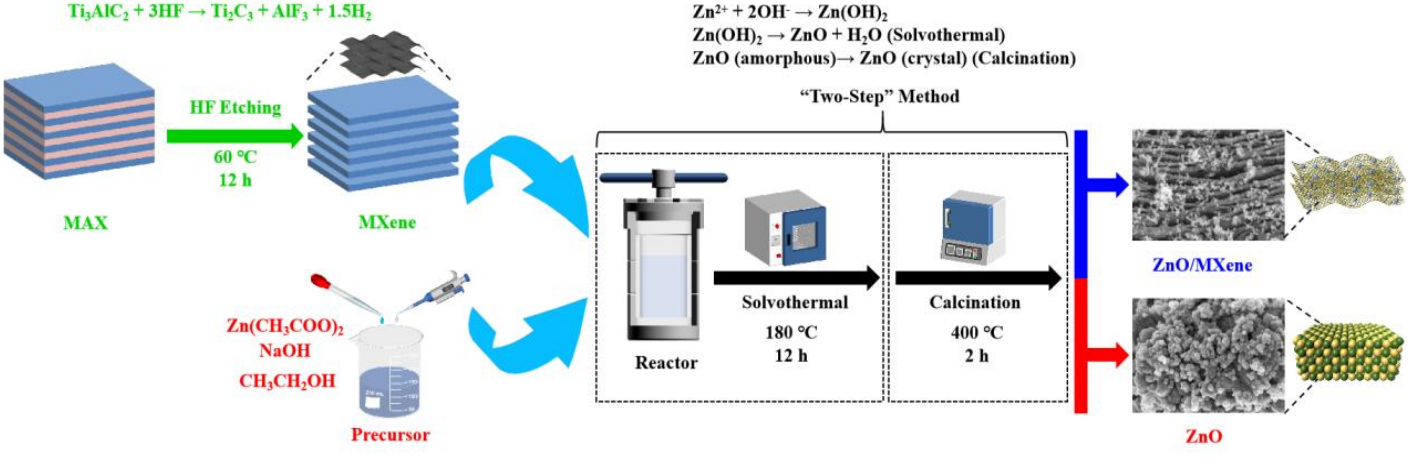

Scheme. 1: Synthetic route illustration of the ZnO/MXene catalyst.

W laser at a wavelength of 325 nm for excitation to measure the crystal structure of the catalyst. The UV-vis diffuse reflectance spectra (UV-vis DRS) of the samples were measured using a UV-vis spectrophotometer (UV3600PLUS, Japan) to analyze the response to UV-visible light. XPS was performed using a Thermo ESCALAB 250Xi system with an Al Kα X-ray source to qualitatively and quantitatively analyze the elemental composition, elemental content, and their chemical states on the catalyst surface.

2.4 Photocatalytic activity test

The ZnO/MXene composite photocatalyst was evaluated based on the photocatalytic degradation of MO and *p*-NP in aqueous solution under simulated sunlight. Twenty milligrams of the photocatalyst were mixed with MO and *p*-NP solutions at an appropriate concentration of 20 $mg \cdot L^{-1}$, respectively. A magnetic stirring rotor was added to the quartz tube containing the mixture. The suspension was magnetically stirred for about 1 hour in the dark and then placed into the photocatalytic reaction apparatus for illumination. At regular intervals, 1 mL aliquots were taken and centrifuged to remove particles. The filtrate was analyzed by recording the changes in the maximum absorption peaks of MO and *p*-NP (520 nm for MO and 312 nm for *p*-NP) using a UV-2550PC UV-visible spectrophotometer. The removal rates of MO and *p*-NP were calculated using the following Eq. (1):

$$R = (C_0 - C_t) \times 100\% \quad (1)$$

where C_0 is the initial mass concentration of MO or *p*-NP in water, and C_t is the mass concentration of contaminants in water after reaction time t. Based on the relationship between absorbance and concentration, the concentrations of MO and *p*-NP were calculated according to the Lambert-Beer law.

The variation of the simulated pollutants concentration with photocatalytic degradation time conformed to the pseudo-first-order kinetics equation,[13] as shown in the following Eq. (2):

$$ln(C_t/C_0) = -k_{1app} \cdot t + b_1 \quad (2)$$

where k_{1app} (min^{-1}) is the degradation kinetic coefficient, t is the reaction time, C_0 ($mg \cdot L^{-1}$) is the initial mass concentration of MO or *p*-NP in water, C_t ($mg \cdot L^{-1}$) is the mass concentration of pollutants in water after reaction time t, and b_1 is the model constant.

The variation of the simulated pollutant concentration with photocatalytic degradation time conformed to the pseudo-second-order kinetics equation, as shown in the following Eq. (3):

$$1/C_t = -k_{2app} \cdot t + b_2 \quad (3)$$

where k_{2app} ($(mg/L)^{-1} \cdot min^{-1}$) is the degradation kinetic coefficient, t is the sampling time, C_0 ($mg \cdot L^{-1}$) is the initial mass concentration of MO or *p*-NP in water, C_t ($mg \cdot L^{-1}$) is the mass concentration of pollutants in water after reaction time t, and b_2 is the model constant.

2.5 Calculation biotoxicity

Developmental toxicity, Mutagenicity, Bioaccumulation factor and concentration of compounds that cause 50% death in oral rats (Rat oral LD_{50} ($mg \cdot kg^{-1}$)) were assessed by the Toxicity Estimation Software Tool (T.E.S.T.) based on quantitative structure-activity relationship (QSAR) model.[14] Parameters used were Developmental toxicity, Mutagenicity, Bioaccumulation factor, Rat oral LD_{50} ($mg \cdot kg^{-1}$), subsequently, "predicted value" was defined as obtained values.[15]

2.6 Gaussian computation

Electrostatic potential (ESP) of MO, degradation intermediates (MO-DPs), *p*-NP and degradation intermediates (*p*-NP-DPs) were calculated by GaussView (version 6.0.16). ESP maps are the changes in electron density distributions throughout the molecule.[16] Colour gradients from red to violet represent the increasing potential distribution,[17] with red regions more electronegative regions than yellow regions.[18] Positive potential regions are highlighted with blue colour, whereas green regions are neutral regions.

Frontier Molecular Orbital (FMO) are expressed in terms of the highest occupied molecular orbital (E_{HOMO}) and lowest unoccupied molecular orbital (E_{LUMO}), and the difference in these energies ΔE determine the stability of molecules. Electron donating capacity is the E_{HOMO}, while electron-accepting is the E_{LUMO}.[19,20] The energy gap is a consequence of the excitation energy of the molecule responsible for transition with low electron density, and the tendency to accept electrons is a measure of the electrophilicity index.[21] E_{HOMO}, E_{LUMO}, energy gap, ionization potential, electron affinity, chemical hardness, chemical softness, electronegativity, chemical potential and electrophilicity index parameters were calculated.

3. Results and discussion

3.1 Physicochemical property of photocatalysts

The SEM characterization results of MXene are shown in Figs. 1a-b, and those of MAX are shown in Figs. S1a-b. After HF etching, the Al layer in Ti_3AlC_2 is etched away, and MXene with a lamellar structure is obtained. The MAX before etching has no inter-layer spacing, while the inter-layer spacing of the etched MXene is about 35-100 nm. The formation of the inter-layer spacing increases, and layer gaps appear, which proves that this is a typical 2D material with a layered structure. The SEM results of ZnO are shown in Figs. 1c-d. ZnO nanoparticles are almost all polymerized spheres with a particle size of about 25-40 nm, a relatively uniform particle size distribution, and a relatively large specific surface area. Moreover, the structure of ZnO nanoparticles is loose, with many voids, and the dispersion degree is good. The SEM results of the ZnO/MXene composite are shown in Figs. 1e-f. The composite material still has a lamellar structure, and the polymeric spherical ZnO nanoparticles can be clearly seen

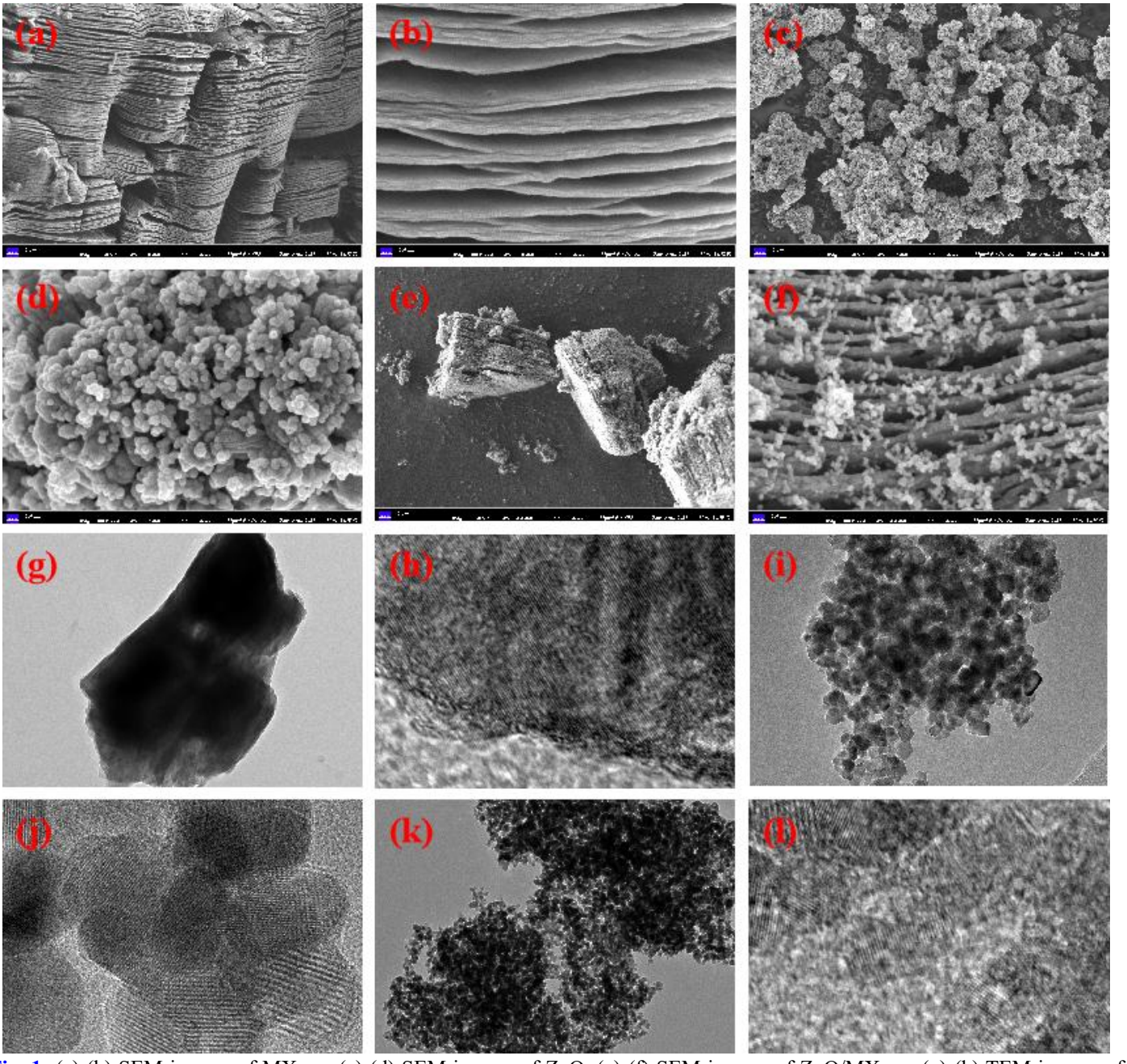

Fig. 1: (a)-(b) SEM images of MXene, (c)-(d) SEM images of ZnO, (e)-(f) SEM images of ZnO/MXene, (g)-(h) TEM images of MXene, (i)-(j) TEM images of ZnO and (k)-(l) TEM images of ZnO/MXene.

covering the surface layer, edges, and inter-layer gaps of the layered structure. The inter-layer spacing of MXene and the particle size of ZnO do not change. This indicates that ZnO nanoparticles were successfully loaded onto MXene to form a sandwich type novel composite photocatalyst, suggesting that the composite was successfully prepared. The successfully prepared ZnO/MXene may exhibit the nanoconfinement effect. Meanwhile, there exists an interface effect between ZnO and MXene. Therefore, based on the synergistic effect of the nanoconfinement-interface effect, its photocatalytic activity is enhanced.

The TEM characterization results of MXene are shown in Figs. 1g-h and Fig. S2a. The obvious layered structure of MXene, with typical lattice stripes, is consistent with the SEM image analysis. Figs. 1i-j show the TEM characterization results of ZnO. It can be seen that ZnO nanoparticles exhibit an obvious polymeric spherical shape, which is consistent with the SEM image analysis. The TEM characterization results of ZnO/MXene are shown in Figs. 1k-l and Fig. S2b. The composite has typical lattice stripes, and the surface layer of the layered structure can be seen to be covered with polymeric spherical ZnO nanoparticles, which is consistent with the SEM image analysis. TEM images of ZnO/MXene with different proportions are shown in Figs. S3-S6. It can be observed that the number of ZnO particles in ZnO/MXene increases significantly with the increase in the proportion.

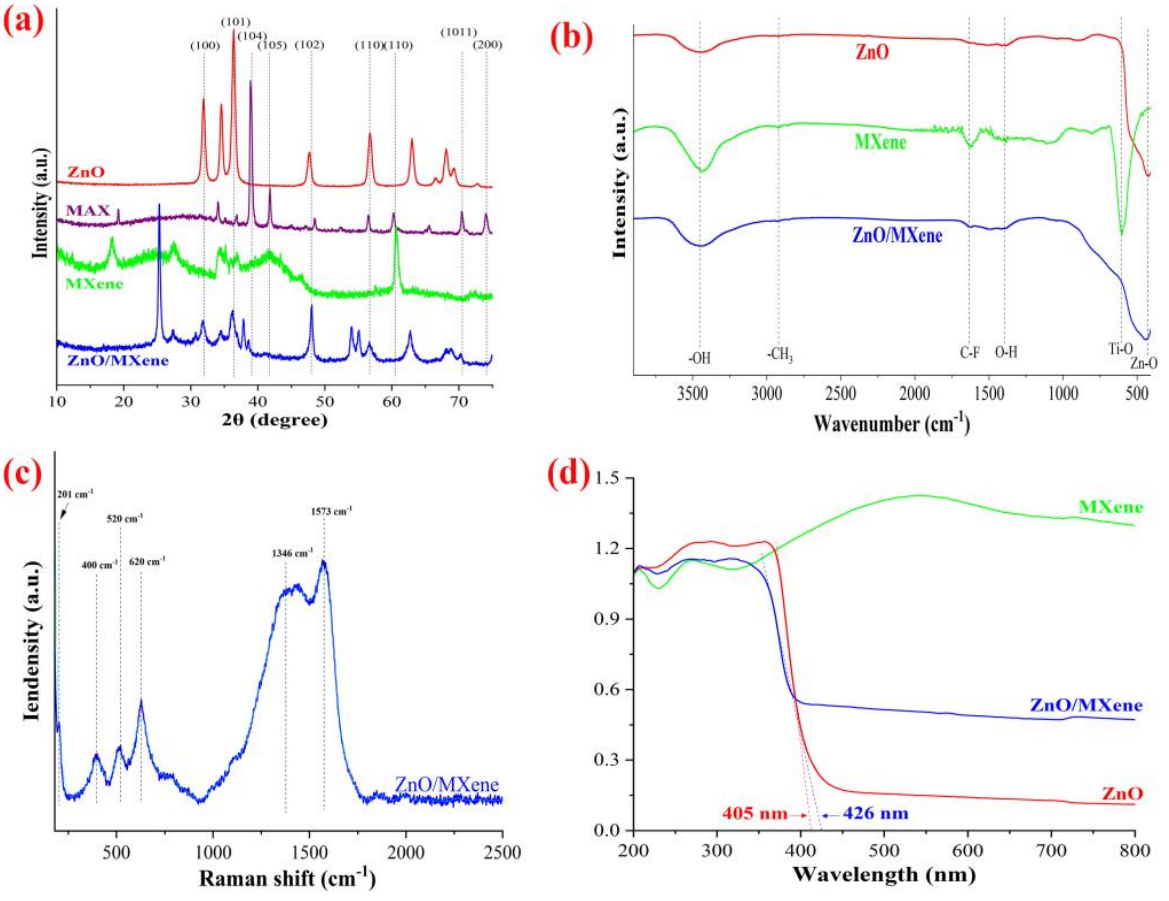

Fig. 2: (a) XRD, (b) FTIR, (c) Raman, (d) ultraviolet-visible (UV-Vis) spectroscopy of samples.

The EDS results of MXene, ZnO, and ZnO/MXene are shown in Tables S1-S3. The theoretical molar ratio of Ti to C in MXene is 1.15:1, while the actual molar ratio of Ti to C is 1.88:1. The data are relatively close, indicating that a pure MXene material was prepared in this study. The theoretical molar ratio of Zn to O in ZnO is 1:1, while the actual molar ratio of Zn to O is 1.25:1. The data are relatively close, indicating that a pure ZnO material was prepared in this study. The ZnO/MXene composite only contains C, O, Ti, and Zn elements, without other impurities. All Zn elements in ZnO/MXene come from ZnO, and all Ti comes from MXene. These results show that ZnO can be successfully loaded onto MXene by the solvothermal method adopted in this experiment, indicating that the composite material was successfully prepared.

The results of the X-ray diffraction patterns of ZnO, MXene, MAX, and ZnO/MXene are shown in Fig. 2a. The XRD pattern of ZnO is consistent with the data from PDF card no. 01-070-8070. The diffraction peaks indicate that the synthesized material has a hexagonal wurtzite ZnO crystal structure. The peaks at 2θ = 31.8°, 34.4°, 36.3°, 47.6°, 56.6°, 62.9°, 66.4°, 68.0°, 69.1°, and 72.6° correspond respectively to the (100), (002), (101), (102), (110), (103), (200), (112), (201), and (004) crystal planes. The sharp peaks indicate good crystallinity of the ZnO material, and no excess impurity peaks are found, which suggests that the prepared ZnO nanoparticles have high purity. The XRD pattern of MAX is consistent with the data from PDF card number 00-052-0875.[22] The diffraction peaks at 2θ = 9.5°, 19.1°, 34.0°, 36.9°, 38.7°, 38.9°, 41.8°, 48.7°, 56.5°, 60.2°, 65.6°, 70.5°, and 74.0° correspond to the (002), (004), (101), (103), (008), (104), (105), (107), (108), (109), (110), (1011), and (200) crystal planes. After etching, the intensity of the (104) characteristic peak of Al at 2θ = 38.9° is weakened. However, the intensity of the (002) crystal plane peak of MXene increases and shifts, and a broad peak is formed at 18.8°. Meanwhile, the XRD pattern of MXene shows that there is a diffraction peak at 2θ = 27.4°, which is not present in the XRD pattern of MAX. All these changes indicate that Al has been removed from Ti_3AlC_2 and MXene has been successfully prepared. The diffraction peaks of ZnO/MXene at 2θ = 25.3°, 31.8°, 34.4°, 36.2°, 37.8°, 48.0°, 54.0°, 55.1°, 56.6°, and 62.7° correspond to the (101), (100), (102), (101), (004), (200), (105), (211), (110), and (103) planes, and the diffraction peak at 2θ = 27.4° corresponds to the XRD pattern of MXene, likely originating from the diffraction peaks of MXene. The diffraction peaks at 2θ = 31.8°, 34.4°, 36.2°, 48.0°, 56.6°, and 62.7° all originate from ZnO, and the diffraction peaks at 2θ = 25.3°, 37.8°, 54.0°, and 55.1° are new diffraction peaks in the XRD pattern of ZnO/MXene. This may be caused by the interface effect of the ZnO/MXene composite, indicating that the preparation of ZnO/MXene was successful.

The infrared spectral image results of ZnO, MXene, and the ZnO/MXene composite are shown in Fig. 2b. It can be observed that for ZnO, a characteristic peak is present at 430 cm^{-1}, which is attributed to the stretching vibration of the Zn-O bond. Additionally, another characteristic peak appears at 3460 cm^{-1}, which is caused by the stretching vibration of -OH.[23] The FTIR spectra of MXene exhibit peaks at 3460 cm^{-1}, 2920 cm^{-1}, 1630 cm^{-1}, 1400 cm^{-1}, and 600 cm^{-1}. These peaks correspond, respectively, to the characteristic absorption peaks of -OH, $-CH_3$, C-F, O-H, and Ti-O bonds.[24] The ZnO/MXene composite is rich in surface functional groups, including -OH (3460 cm^{-1}), $-CH_3$ (2920 cm^{-1}), O-H (1630 cm^{-1}), and Zn-O (430 cm^{-1}). These results indicate the successful preparation of the composite.

The Raman spectral image results of MXene and the ZnO/MXene composite are shown in Fig. 2c and Fig. S7. The characteristic Raman bands located at 201 cm^{-1} and 620 cm^{-1} are assigned to the A1g symmetric out-of-plane vibration of Ti atoms and the Eg group vibration of the surface functional group atoms, respectively.[25,26] More importantly, the overlapping peak at 1346 cm^{-1} can be attributed to the carbon structural defects caused by disordered sp^3 C atoms (band D), while the peak at 1573 cm^{-1} can be attributed to the graphite layer of sp^2 mixed C atoms (band G),[27] which is consistent with the results shown in Fig. S7. The results indicate that MXene is present in the ZnO/MXene composites.

The UV-vis absorption spectral image results of ZnO, MXene, and ZnO/MXene composite are shown in Fig. 2d and Fig. S8. ZnO exhibits a strong response to ultraviolet (UV) light with a wavelength shorter than 390 nm. However, its response is relatively low when the wavelength of visible light exceeds 390 nm. In the UV-visible region, the spectrum shows a sharp fundamental absorption, and there is a band-gap absorption edge at 405 nm. This is due to the band-gap absorption caused by the electronic transition from the valence band to the conduction band of ZnO. After calculation, the band gap width of ZnO nanoparticles is determined to be 3.06 eV. MXene shows a strong response to light within the wavelength range of 250 to 800 nm, which can be attributed to the darker color inherent to MXene itself. The ZnO/MXene composite has a strong response to UV light with wavelengths shorter than 350 nm, but a weak response in the visible light range with wavelengths longer than 390 nm. The spectrum of the composite exhibits strong absorption in the UV-visible region, with a bandgap absorption edge at 426 nm. Based on the calculation, the band gap width of the ZnO/MXene composite is 2.91 eV. In the wavelength region above 400 nm, the response of the ZnO/MXene composite to visible light is approximately 200% stronger than that of the ZnO photocatalyst. This phenomenon may be associated with the unique properties of the 2D material MXene itself. The presence of carbon can effectively adjust the band gap width of semiconductor materials.[28] Meanwhile, the UV-Vis absorption spectra indicate that the ZnO/MXene composite photocatalyst has been successfully prepared.

The results of the XPS full spectra of ZnO, MXene, and the ZnO/MXene composite are shown in Fig. S9. ZnO consists of Zn, O, and C elements, and the Zn2p, O1s, and C1s orbitals are detected. The content of the Zn element is 15.38%, the content of the O element is 58.65%, and the content of the C element is 25.97%. MXene contains Ti, O, and C elements, and the characteristic Ti2p orbital is observed. The content of the Ti element is 24.12%, the content of the O element is 11.68%, and the content of the C element is 56.23%. The ZnO/MXene composite photocatalyst contains Zn, Ti, O, and C elements, and the Zn2p, Ti2p, O1s, and C1s orbitals are present simultaneously. The content of the Zn element is 18.4%, that of the Ti element is 5.68%, that of the O element is 56.37%, and that of the C element is 19.55%. These results indicate that the ZnO/MXene composite photocatalyst has been successfully prepared. The peak fitting results of C1s are shown in Fig. 3a. MXene exhibits diffraction peaks at 282.2 eV and 284.8 eV. The peak at 282.2 eV corresponds to the C-Ti bond, and the peak at 284.8 eV corresponds to the C-C bond. In contrast, ZnO has diffraction peaks at 288.3 eV, 286.1 eV, and 284.7 eV. These peaks correspond to the O-C=O, C=O, and C-C bonds, respectively. The ZnO/MXene composite shows diffraction peaks at 288.9 eV and 284.8 eV. Among them, the functional group corresponding to the peak at 288.9 eV originates from the O-C=O bond of ZnO, and the functional group corresponding to the peak at 284.8 eV comes from either the C-C bond of MXene or that of ZnO. The peak fitting results of O1s are shown in Fig. 3b. ZnO exhibits diffraction peaks at 531.4 eV and 529.9 eV. The main peak at 529.9 eV in ZnO is associated with the lattice oxygen (O^{2-}) in the Zn-O bond, while the main peak at 531.4 eV is related to the chemically adsorbed oxygen (-OH). In MXene, the main peak at 530.1 eV is associated with the Ti-O bond, and the main peak at 532.1 eV is related to -OH.[29] For the ZnO/MXene composite, diffraction peaks at 530.1 eV and 531.4 eV are observed. Among them, the functional group corresponding to the peak at 530.1 eV originates from the Ti-O bond of MXene, and the peak at 531.4 eV is associated with the chemisorbed oxygen (-OH) of ZnO, which indicates the successful synthesis of the composite material. The peak fitting results of Ti2p are shown in Fig. 3c. MXene exhibits diffraction peaks at 461.4 eV and 455.4 eV, which correspond to the C-Ti-F bond and the Ti-C bond, respectively.[30] The presence of the F element may be attributed to the extensive use of HF during the etching process, which leads to the formation of the Ti-F bond in MXene. The energy difference between these two bonds is within the range of 6.0 eV.For the ZnO/MXene composite, diffraction peaks at 475.2 eV, 464.2 eV, and 458.4 eV are observed. Among them, the peak at 475.2 eV corresponds to the Ti-O-Zn functional group, indicating that the composite contains Ti, O, and Zn elements, which provides evidence for the successful synthesis of the composite. The energy difference between the two diffraction peaks at 464.2 eV and 458.4 eV is 5.8 eV, which is similar to the energy difference range of the diffraction peaks in MXene

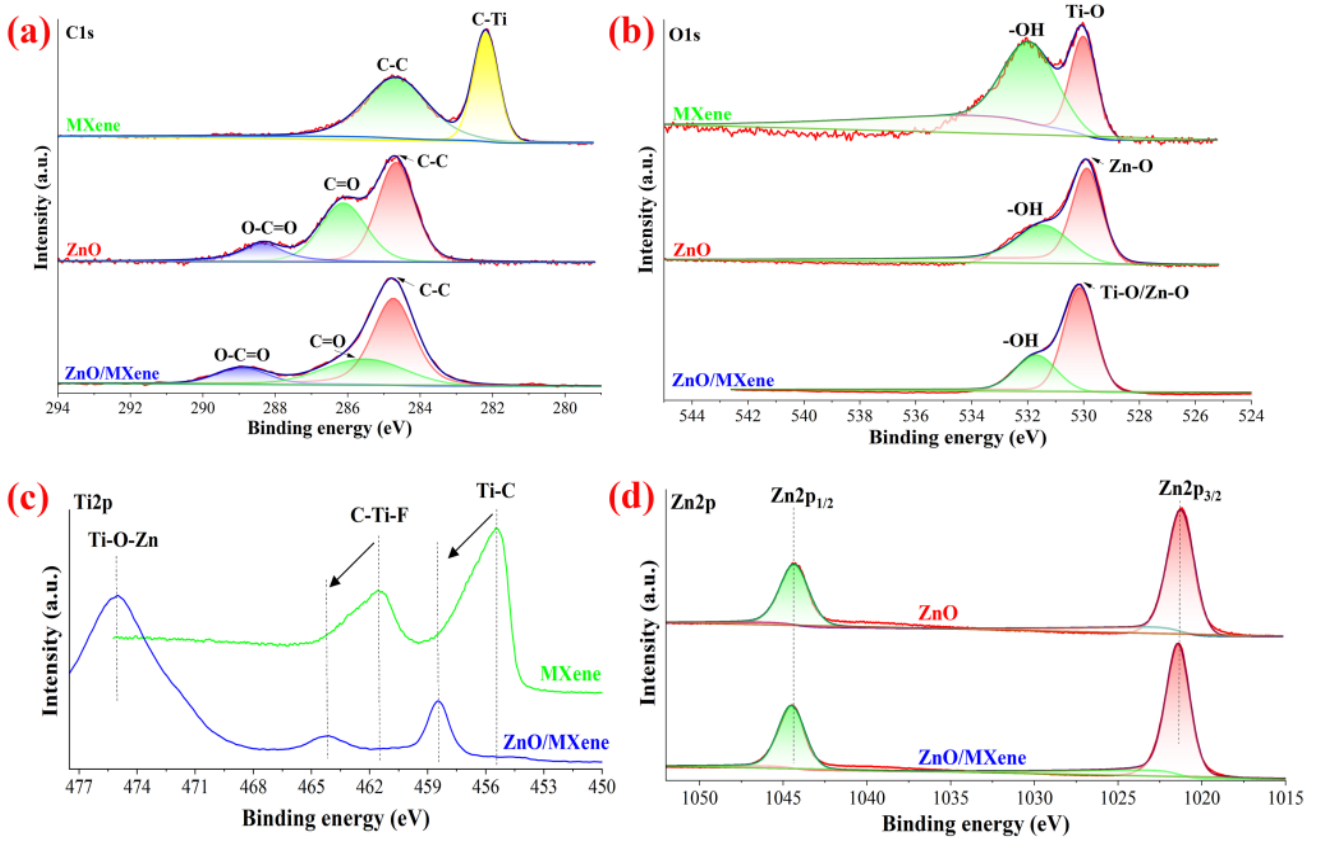

Fig. 3: XPS spectra of (a) C1s, (b) O1s, (c) Ti2p and (d) Zn2p elements in MXene, ZnO and ZnO/MXene.

and corresponds to the C-Ti-F bond and Ti-C bond in MXene. However, these two diffraction peaks exhibit a red shift, suggesting that the material has been successfully composited and an interface effect has been generated simultaneously. The peak fitting results of Zn2p are shown in Fig. 3d. The Zn2p spectra of ZnO and the ZnO/MXene composite exhibit diffraction peaks at 1044.7 eV and 1021.5 eV. The binding energy ranges for both ZnO and the ZnO/MXene composite are 23.2 eV, and the spacing remains unchanged. This indicates that all the Zn elements in the ZnO/MXene composite originate from ZnO.

3.2 Photocatalytic activity of photocatalysts

As shown in Fig. S10a-b and Table S4, the highest removal rate of MO is 11.05%, while the highest removal rate of *p*-NP is 5.66%. The photodegradation rate of MO is higher than that of *p*-NP, and the removal rates of both substances increase with time. The pseudo-first-order and pseudo-second-order kinetics constants are 0.0007 min^{-1} and 0.00004 $(mg/L)^{-1}\cdot min^{-1}$ for MO, and 0.0003 min^{-1} and 0.00002 $(mg/L)^{-1}\cdot min^{-1}$ for *p*-NP, respectively. The values for MO are all greater than those for *p*-NP, indicating that the degradation rate of MO is higher than that of *p*-NP.

The change curve of the MO removal rate with the reaction time at different mass ratios of ZnO to MXene is shown in Fig. 4a. Without adding photocatalyst, the removal rate of MO is very low and can be neglected. In the five groups of experiments using the ZnO/MXene composite, the removal rate of MO is significantly improved. Analysis of the five group experimental data shows that the removal efficiency of MO first increases and then decreases as the mass ratio of ZnO to MXene increases.When the mass ratio is less than 1:1, the degradation performance improves with the increase of the mass ratio. When the mass ratio is greater than 1:1, the degradation performance decreases significantly as the mass ratio increases. At a mass ratio of 1:1, the ZnO/MXene composite has the best degradation effect on MO, and the removal rate can reach 100% after 150 minutes of reaction.

The curve showing the change in the *p*-NP removal rate with reaction time at different mass ratios of ZnO to MXene is presented in Fig. 4b. Without a photocatalyst under UV irradiation, the degradation rate of *p*-NP is extremely low and can be ignored. By analyzing the five sets of experimental data, we can observe that the removal rate of *p*-NP first increases and then decreases as the mass ratio of ZnO to MXene increases.When the mass ratio is less than 1:1, the degradation performance improves as the mass ratio increases. When the mass ratio is greater than 1:1, the degradation performance decreases significantly as the mass ratio rises. At a mass ratio of 1:1, the ZnO/MXene composite has the best degradation effect on *p*-NP, and the removal rate can reach 74% after 180 minutes of reaction. The results indicate that the ZnO/MXene composite also has a good degradation effect on *p*-NP, and the optimal mass ratio is 1:1. The curve depicting the change in

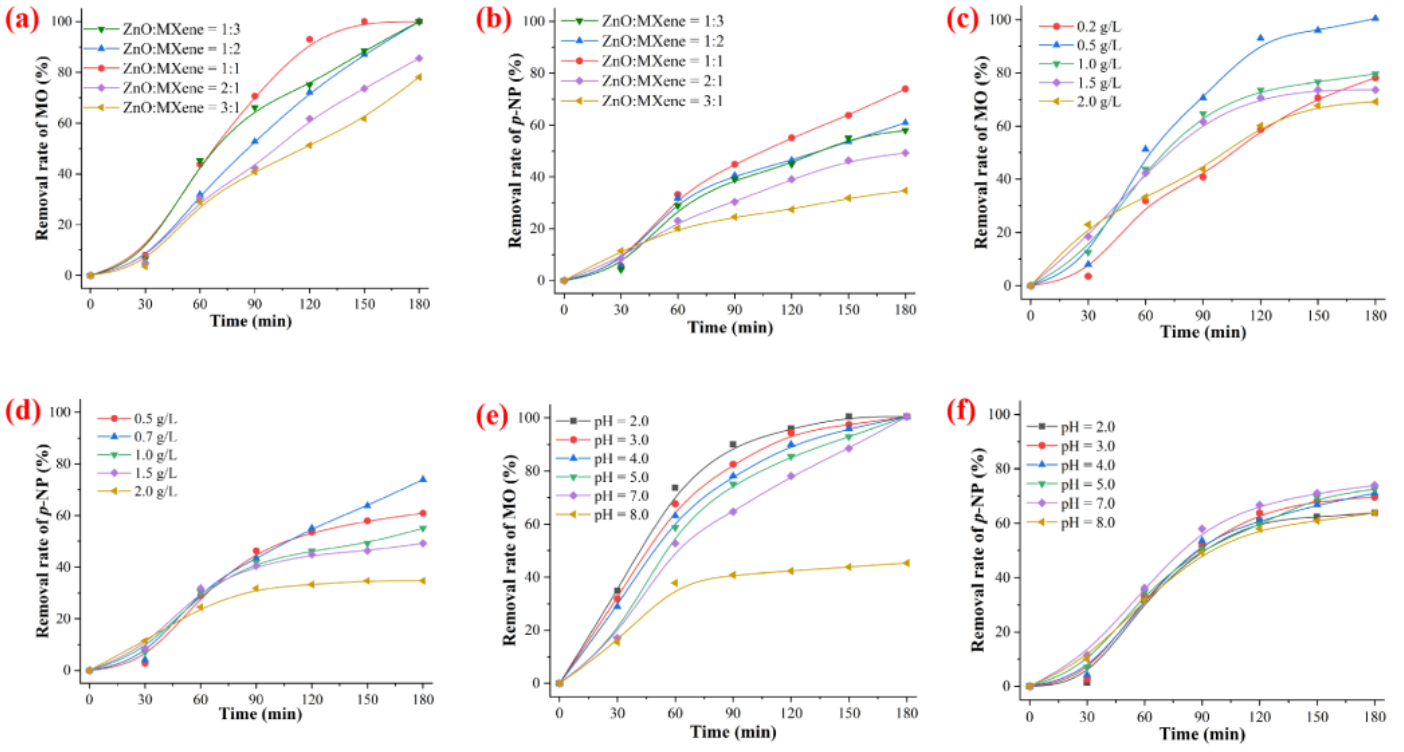

Fig. 4: The effect of mass ratio for MO (a) and *p*-NP (b), dosage for MO (c) and *p*-NP (d), and pH for MO (e) and *p*-NP (f) on photocatalytic performance of ZnO/MXene.

the MO removal rate as a function of the dosage of ZnO and MXene over the reaction time is shown in Fig. 4c. In the first 30 minutes in the dark, the removal rate of MO increased with the increasing dosage of the ZnO/MXene composite catalyst. After 30 minutes under ultraviolet light irradiation, the removal efficiency of MO first increased and then decreased as the dosage of the ZnO/MXene composite increased.When the dosage was less than 0.5 $g \cdot L^{-1}$, the degradation performance improved with the increase in dosage. When the dosage was greater than 0.5 $g \cdot L^{-1}$, the degradation performance decreased as the dosage increased. When the dosage of the ZnO/MXene composite was 0.5 $g \cdot L^{-1}$, the removal rate of MO was the highest, and it could reach 100% after 180 minutes of reaction. This removal rate was significantly higher than those of the other four groups of experiments. These results indicate that the ZnO/MXene composite has a good degradation effect on MO, and the optimal dosage in the degradation test is 0.5 $g \cdot L^{-1}$. The curve showing the effect of the dosage of ZnO and MXene on the removal rate of *p*-NP over the reaction time is presented in Fig. 4d. In the first 30 minutes in the dark, the removal rate of *p*-NP increased as the dosage of the ZnO/MXene composite catalyst increased. After 30 minutes, under ultraviolet light irradiation, the removal efficiency of *p*-NP first increased and then decreased with the increasing dosage of the ZnO/MXene composite.When the dosage was less than 0.7 $g \cdot L^{-1}$, the degradation performance improved as the dosage increased. When the dosage is greater than 0.7 $g \cdot L^{-1}$, the degradation performance decreases as the dosage increases. At a dosage of 0.7 $g \cdot L^{-1}$, the ZnO/MXene composite has the best degradation effect on *p*-NP, and the removal rate can reach 74% after 180 minutes of reaction. The experimental results indicate that the ZnO/MXene composite material has a good degradation effect on *p*-NP, and the optimal dosage in the degradation test is 0.7 $g \cdot L^{-1}$. The curve showing the change in the MO removal rate as a function of reaction time at different pH values is presented in Fig. 4e. The ZnO/MXene composite material exhibits a better degradation effect under acidic and neutral conditions. When the pH = 2.0, the MO removal rate can reach 100% after 150 minutes of reaction. As the pH value increases, the MO removal rate decreases, although the decrease is not significant. The MO removal rate can still reach 100% after 180 minutes. The degradation efficiency of the ZnO/MXene composite drops sharply under alkaline conditions. At pH = 8.0, the MO removal rate reaches 45.32% after 180 minutes of reaction. This is because MO is an anionic dye, which is not easily adsorbed and degrades poorly under alkaline conditions.

The curve of the *p*-NP removal rate as a function of reaction time at different pH values is shown in Fig. 4f. As the pH value increases, the removal rate of *p*-NP first increases and then decreases. When the pH is less than 7, the degradation performance improves gradually with the increase in pH. When the pH is greater than 7, the degradation performance decreases significantly with the increase in pH. At a pH of 7, the ZnO/MXene composite has the best degradation effect on *p*-NP, and the removal rate can reach 74% after 180 minutes of reaction. The pseudo-first-order kinetics and pseudo-second-order kinetics results of the photocatalytic

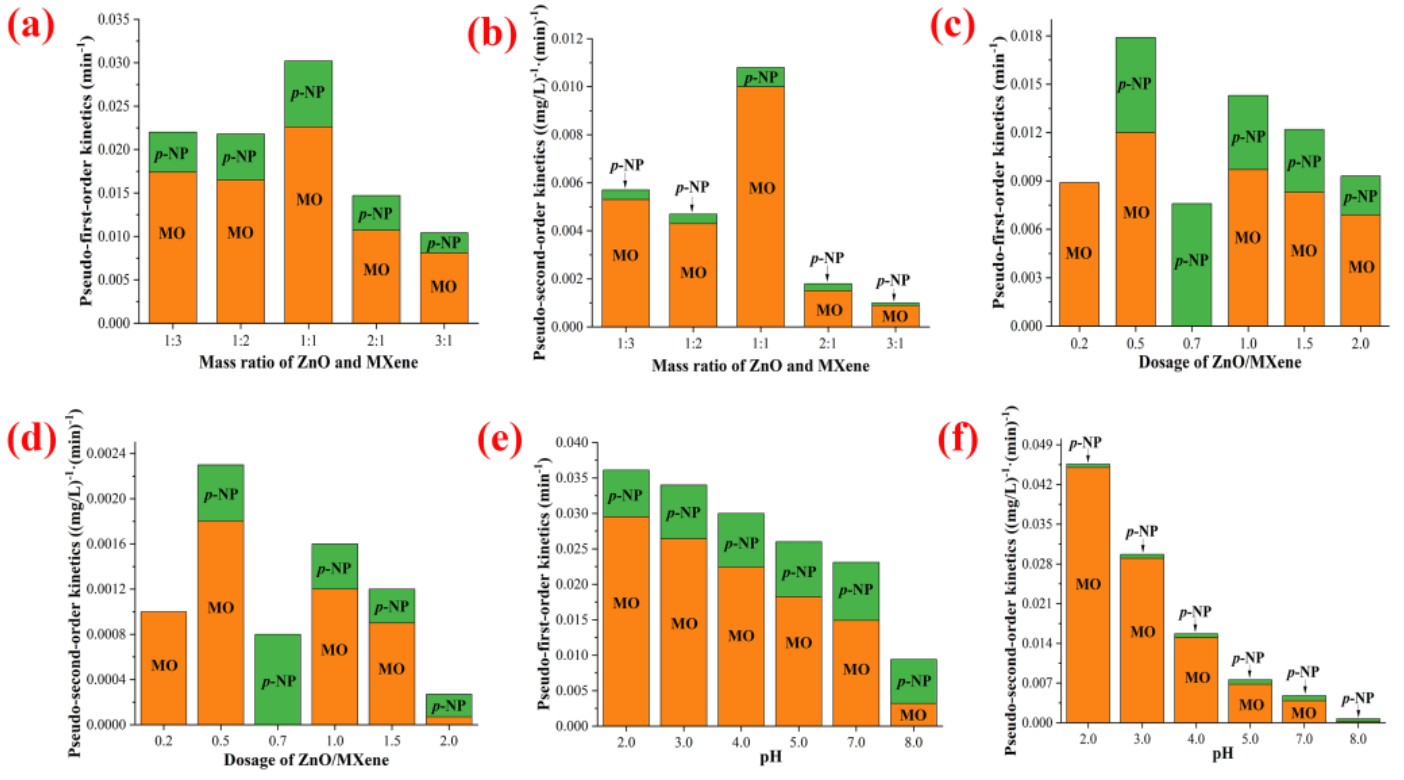

Fig. 5: The effect of mass ratio for pseudo-first-order kinetics (a) and pseudo-second-order kinetics (b), dosage for pseudo-first-order kinetics (c) and pseudo-second-order kinetics (d), and pH for pseudo-first-order kinetics (e) and pseudo-second-order kinetics (f) on photocatalytic performance of ZnO/MXene.

degradation of MO and *p*-NP using the ZnO/MXene composite with different mass ratios as the photocatalyst are shown in Figs. 5a-b and Tables S5-S6. When the mass ratio of ZnO to MXene in the composite is 1:1, the pseudo -first-order kinetic constant for MO degradation is 0.0226 min^{-1}, while for the remaining ratios, the constants range from 0.0007 min^{-1} to 0.0174 min^{-1}. The pseudo-first-order kinetics constant for *p*-NP degradation is 0.0076 min^{-1}, and for the other ratios, the constants range from 0.0003 min^{-1} to 0.0053 min^{-1}. The degradation rate of MO is higher than that of *p*-NP, indicating that the ZnO/MXene composite has a better degradation effect on MO than on *p*-NP. When the mass ratio of ZnO:MXene is 1:1, the degradation rate is the fastest, which is significantly better than that of the other four groups of materials. The results of pseudo-second-order kinetics were consistent with that of pseudo-first-order kinetics.

Figs. 5c-d and Tables S7-S8 show the results of the pseudo-first-order kinetics and pseudo-second-order kinetics of the photocatalytic degradation of MO and *p*-NP with changes in the dosage of the ZnO/MXene composite. When the dosage of the ZnO/MXene composite is 0.5 $g \cdot L^{-1}$, the pseudo-first-order kinetics constant for MO degradation is 0.012 min^{-1}, and for other dosages, the pseudo-first-order kinetics constants are between 0.0069 min^{-1} and 0.01 min^{-1}. The degradation rate of the ZnO/MXene composite is the fastest at this dosage, which is significantly better than that of the other five groups. When the dosage of the ZnO/MXene composite is 0.7 $g \cdot L^{-1}$, the pseudo-first-order kinetics constant for *p*-NP degradation is 0.0076 min^{-1}, and for other dosages, the pseudo-first-order kinetics constants are between 0.0003 min^{-1} and 0.0059 min^{-1}. The degradation rate of the ZnO/MXene composite is the fastest at this dosage, which is significantly better than that of the other five groups. The results of pseudo-second-order kinetics were consistent with that of pseudo-first-order kinetics.

The results of the pseudo-first-order kinetics and pseudo-second-order kinetics of the photocatalytic degradation of MO and *p*-NP with changes in pH are shown in Figs. 5e-f and Tables S9-S10. At pH = 2.0, the pseudo-first-order kinetics constant for the degradation of MO is 0.0295 min^{-1}, and for other pH values, the pseudo-first-order kinetics constants are between 0.0032 min^{-1} and 0.0264 min^{-1}, indicating that the ZnO/MXene composite has the best degradation effect on MO at pH = 2.0. The removal efficiency of MO decreases as the pH value increases. At pH = 8.0, the pseudo-first-order kinetics constant for the degradation of MO decreases to 0.0032 min^{-1}, indicating the worst degradation effect. The pseudo-first-order kinetics constant for the degradation of *p*-NP at pH = 7.0 is 0.0082 min^{-1}, and for other pH values, the pseudo-first-order kinetics constants are between 0.0062 min^{-1} and 0.0078 min^{-1}, indicating that the ZnO/MXene composite has the best degradation effect on *p*-NP at pH = 7.0. The removal rate of *p*-NP first increases and then decreases as the pH value increases. At pH = 2.0, 3.0, 4.0, 5.0, and 7.0, the

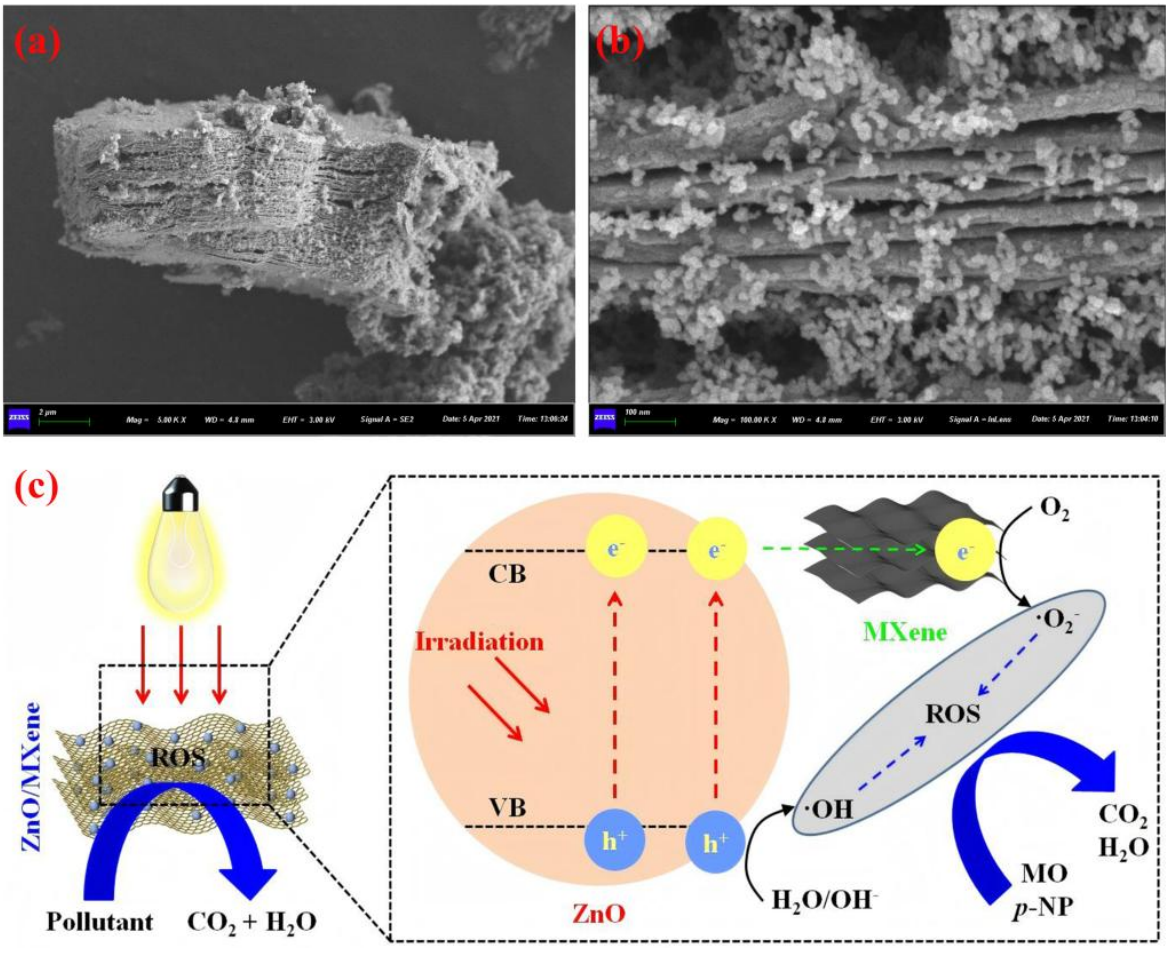

Fig. 6: SEM images of the used ZnO/MXene composite(a)-(b) and the photocatalytic mechanism for degradation of MO and *p*-NP by the ZnO/MXene composite under visible light irradiation (c).

degradation rate of MO is significantly higher than that of *p*-NP. However, at pH = 8.0, the degradation rate of MO is significantly lower than that of *p*-NP. This fully indicates that the ZnO/MXene composite has a better degradation effect on MO than on *p*-NP under acidic or neutral conditions, while the degradation efficiency of MO is lower than that of *p*-NP under alkaline conditions. The results of pseudo-second-order kinetics were consistent with that of pseudo-first-order kinetics.

3.3 Photocatalytic mechanism of ZnO/MXene

The SEM results of the ZnO/MXene composite material after its use are shown in Figs. 6a-b. The structure of the ZnO/MXene composite material remains unchanged after being used, which indicates that the ZnO/MXene composite material still exhibits a good photocatalytic performance and has a long service life even after utilization. Possible photocatalytic mechanisms for the degradation of MO and *p*-NP pollutants are presented in Fig. 6c. Under light irradiation, electrons in the valence band of ZnO absorb energy and are excited to transition to the conduction band. Correspondingly, holes (h^+) are generated in the valence band, forming electron-hole pairs.[31] The holes can react with H_2O and OH^- to form hydroxyl radicals (·OH),[32] and the electrons migrate to the surface of ZnO particles under the action of the space electric field. Subsequently, these electrons migrate to the surface of MXene and react with O_2 to form superoxide radicals ($\cdot O_2^-$).[33] Both ·OH and $\cdot O_2^-$ contribute to the formation of reactive oxygen species (ROS).[34] Due to the nanoconfinement effect of MXene and the interface effect between ZnO and MXene, the constructed 0D/2D ZnO/MXene photocatalytic materials exhibit a significant synergistic effect in the degradation of MO and *p*-NP. This enhances the generation ability of free radicals, endowing them with strong chemical activity. As a result, the ability to degrade MO and *p*-NP organic pollutants is improved, ultimately leading to the generation of CO_2 and H_2O.

3.4 Pollutant degradation process and toxicity calculation

The possible degradation pathways of MO are shown in Fig. 7. They can be divided into four paths. In the first path, the sulfonic acid group is destroyed, and the hydroxyl group replaces the sulfonic acid group to form MO-P1.[35] The carbon-nitrogen bond on the posterior benzene ring is broken, resulting in the formation of MO-P2 and MO-P3. The second path is demethylation. In this process, a -CH_3 group on N is

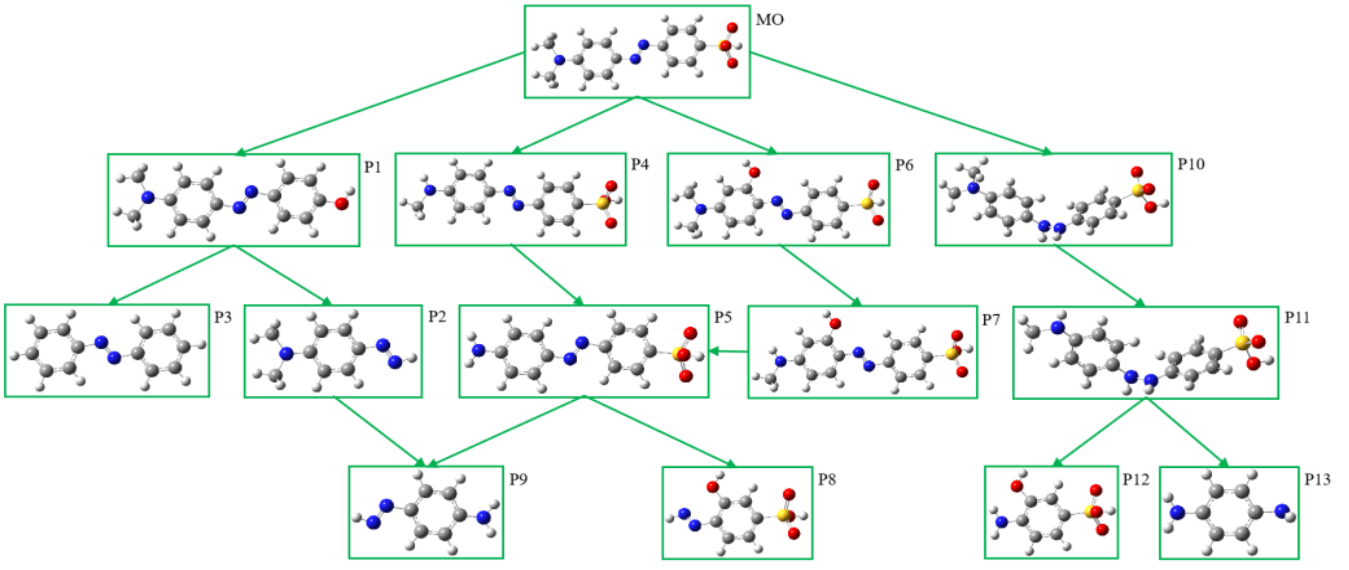

Fig. 7: MO degradation pathway.

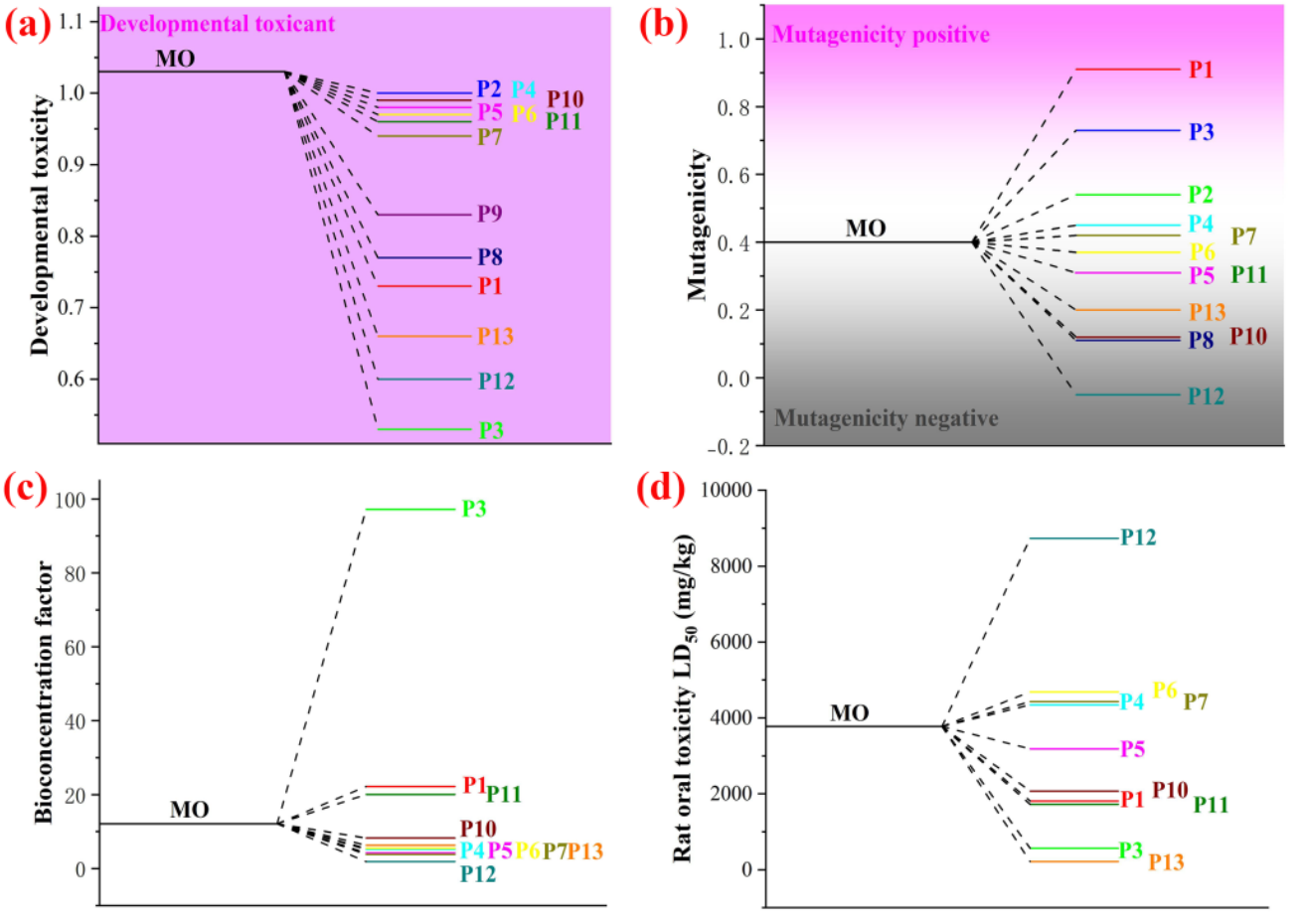

Fig. 8: Developmental toxicity (a), Mutagenicity (b), Bioaccumulation factor (c), Rat oral toxicity LD_{50} ($mg \cdot kg^{-1}$) (d) for MO and MO-DPs.

removed to generate MO-P4, and then another methyl group is removed to obtain MO-P5.[36] After that, the carbon-nitrogen bond on the benzene ring is broken, and the hydroxyl group attacks the benzene ring, generating MO-P8 and MO-P9. The third path is that the hydroxyl group attacks the hydrogen on the benzene ring adjacent to the azo bond, and a substitution reaction occurs to form MO-P6. Then a $-CH_3$ group on the N is removed to obtain MO-P7, and another methyl group is

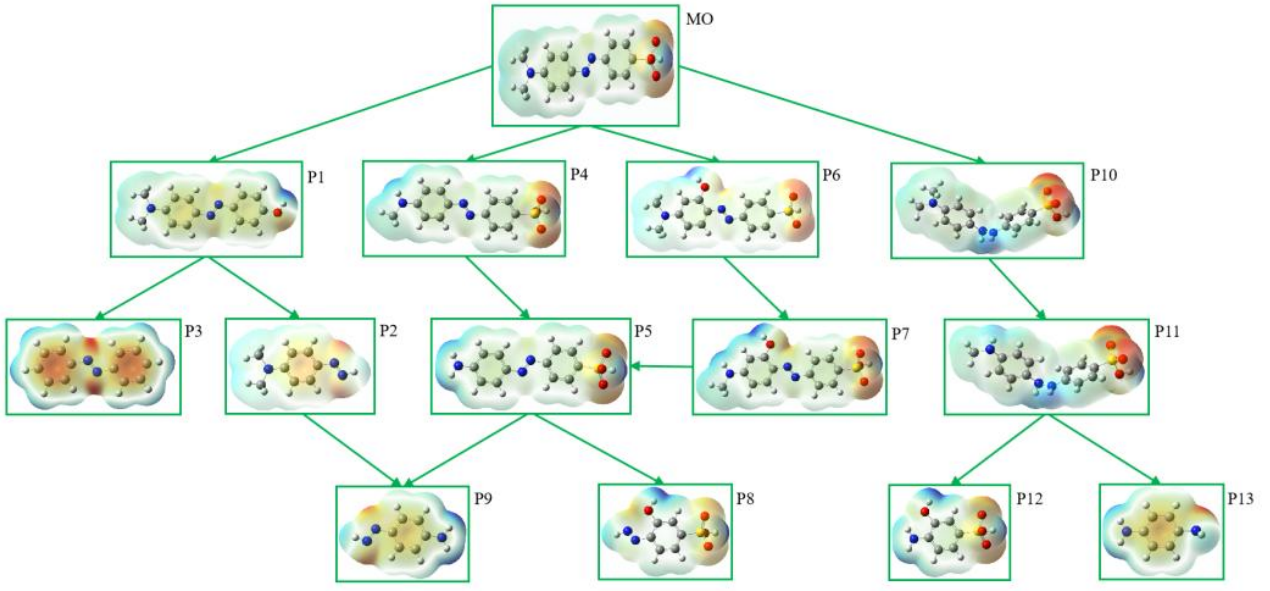

Fig. 9: Bulk electrostatic potential of MO and MO-DPs.

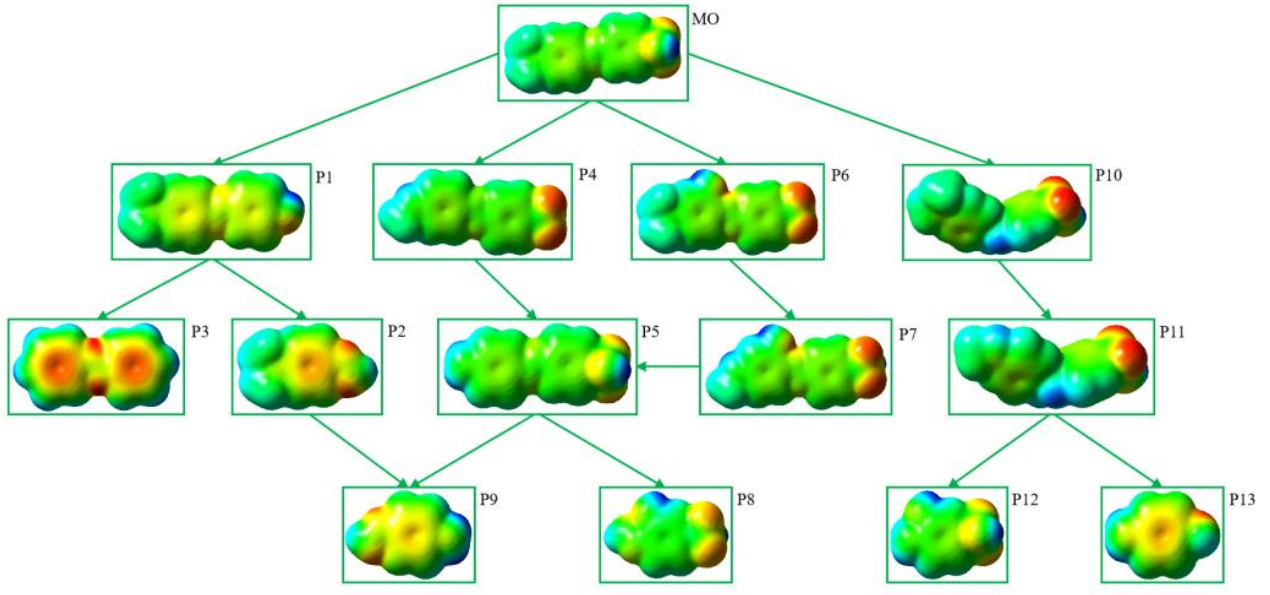

Fig. 10: Surface electrostatic potential of MO and MO-DPs.

removed to obtain MO-P5. Subsequently, the carbon-nitrogen bond on the benzene ring is broken, and the hydroxyl group attacks the benzene ring to form MO-P8 and MO-P9.[37] The fourth path is the breaking of the N=N azo bond to form a HN-NH single bond, resulting in the formation of MO-P10. Then, demethylation occurs, and a -CH_3 group on N is removed to obtain MO-P11. Next, the HN-NH single bond is destroyed, and all methyl groups on the right side of the molecule are detached, transforming it into phenolic organic compounds, and MO-P12 and MO-P13 are obtained respectively. Finally, the low molecular weight organic matter are mineralized into H_2O and CO_2 through the action of free radicals.

The simulated biotoxicity of the degradation products is an important indicator for evaluating the catalyst or the degradation process.[38] The Developmental toxicity, Mutagenicity, Bioaccumulation factor, and Rat oral toxicity LD_{50} ($mg \cdot kg^{-1}$) of MO and the MO degradation products (MO-DPs: P1, P2, P3, P4, P5, P6, P7, P8, P9, P10, P11, P12, P13) in the presence of the ZnO/MXene composite were evaluated through T.E.S.T. calculation. A series of generated MO-DPs intermediates were selected to assess the biotoxicity of the solutions treated during the degradation process of the ZnO/MXene composite. MO and MO-DPs exhibited a "Developmental toxicant" phenotype, whereas ZnO/MXene composite treatment reduced the Developmental toxicity of P1, P2, P3, P4, P5, P6, P7, P8, P9, P10, P11, P12, P13 (Fig. 8a and Table S11). MO and MO-DPs exhibited a "Mutagenicity positive" state, whereas the ZnO/MXene composite treatment reduced the Mutagenicity of P5, P6, P8, P10, P11, P12, P13 and increased the Mutagenicity of P1, P2, P3, P4, P7, but not

of P9 (Fig. 8b and Table S11). The ZnO/MXene composite treatment reduced the Bioaccumulation factor of P1, P2, P3, P4, P5, P6, P7, and P8 (Fig. 8c and Table S11). ZnO/MXene composite treatment reduced Rat oral toxicity LD_{50} ($mg \cdot kg^{-1}$) in P1, P3, P5, P10, P11, 1P13 rats and increased Rat oral toxicity LD_{50} ($mg \cdot kg^{-1}$) in P4, P6, P7, P12 rats (Fig. 8d and Table S11).

The charge distribution can be described by the ESP, and the results of ESP of MO are shown in Figs. 9-10. The presence of red and blue regions can assist us in understanding the charge distribution of molecules in different areas. The charge distribution is crucial for comprehending the position of the bulk phase charge distribution, as well as the reactivity and the mechanisms of electrophilic and nucleophilic reactions.For MO, MO-P4, MO-P5, MO-P6, MO-P7, MO-P8, MO-P10, MO-P11, and MO-P12, the red regions of the ESP represent the S=O and S-O bonds of the sulfonic acid group. The blue regions represent the $-CH_3$ groups, while for MO-P1,

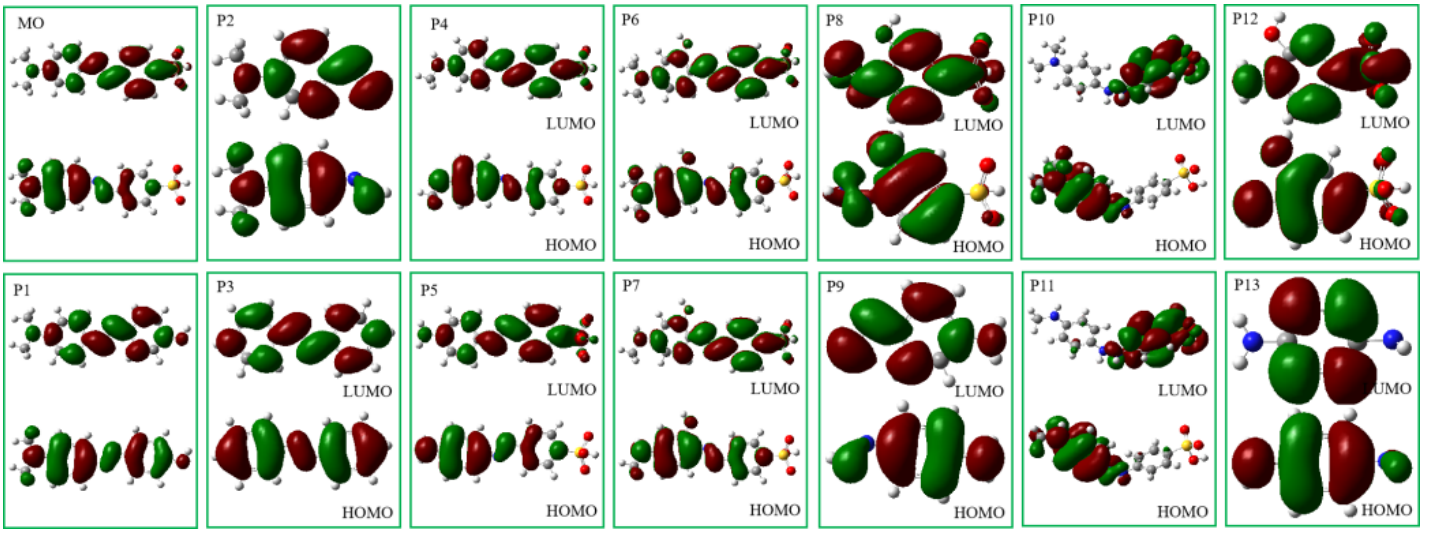

Fig. 11: The changes of E_{HOMO} and E_{LUMO} of MO and MO-DPs.

Table 1: The law of the parameters of the MO orbit.

Name	E_{HOMO}	E_{LUMO}	Energy gap (E_{HOMO}-E_{LUMO})	Ionization potential (I=-E_{HOMO})	Electron affinity (A=-E_{LUMO})	Electron affinity (η=(I-A)/2)	Chemical softness (ζ=1/2η)	Electronegativity (X=(I+A)/2)	Chemical potential (μ=-(I+A)/2)	Electrophilicity index (ω=$μ^2$/2η)
MO	-7.70	1.14	8.85	7.70	-1.14	4.42	0.11	3.28	-3.28	1.22
P1	-7.15	2.19	9.34	7.15	-2.19	4.67	0.11	2.48	-2.48	0.66
P2	-7.51	2.97	10.48	7.51	-2.97	5.24	0.10	2.27	-2.27	0.49
P3	-8.45	1.69	10.14	8.45	-1.69	5.07	0.10	3.38	-3.38	1.13
P4	-7.80	1.14	8.94	7.80	-1.14	4.47	0.11	3.33	-3.33	1.24
P5	-7.94	1.13	9.07	7.94	-1.13	4.54	0.11	3.41	-3.41	1.28
P6	-7.76	1.30	9.05	7.76	-1.30	4.53	0.11	3.23	-3.23	1.15
P7	-7.85	1.29	9.14	7.85	-1.29	4.57	0.11	3.28	-3.28	1.18
P8	-9.65	1.48	11.13	9.65	-1.48	5.57	0.09	4.08	-4.08	1.50
P9	-7.77	2.99	10.75	7.77	-2.99	5.38	0.09	2.39	-2.39	0.53
P10	-7.24	3.00	10.24	7.24	-3.00	5.12	0.10	2.12	-2.12	0.44
P11	-7.36	3.01	10.37	7.36	-3.01	5.19	0.10	2.18	-2.18	0.46
P12	-8.53	2.85	11.38	8.53	-2.85	5.69	0.09	2.84	-2.84	0.71
P13	-7.51	4.31	11.83	7.51	-4.31	5.91	0.08	1.60	-1.60	0.22

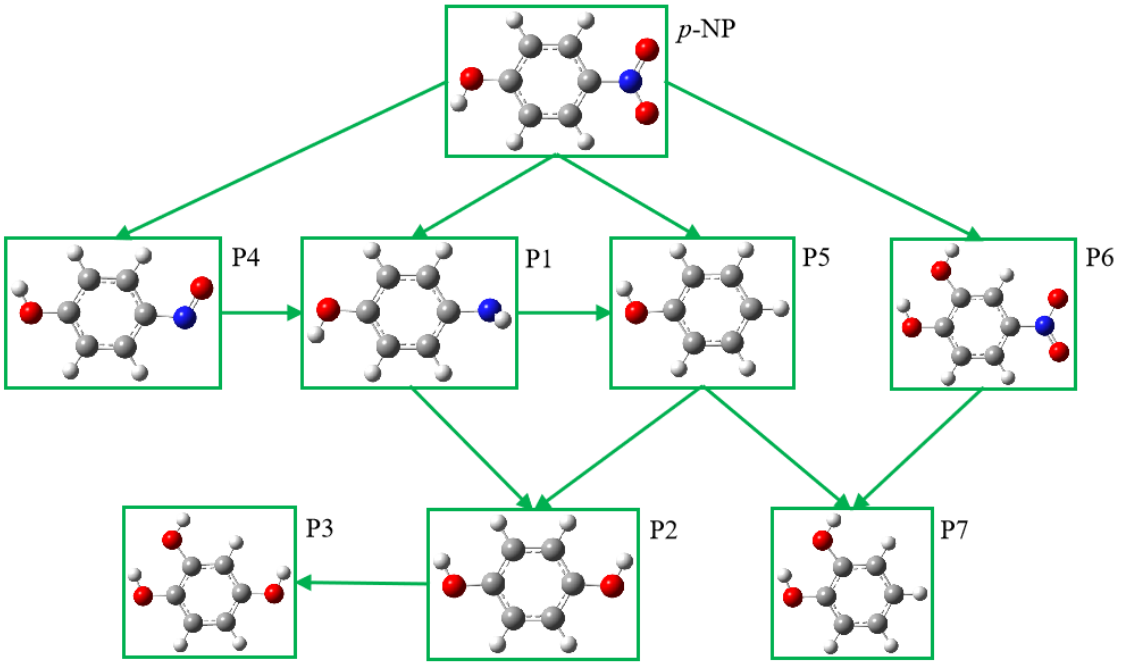

Fig. 12: *p*-NP degradation pathway.

the blue regions represent the O-H bonds. The variation in the surface charge distribution mainly stems from the S=O bond, S-O bond, and the structure and length of the hydrocarbon chain. The regions enriched with negative charges are precisely the red regions.

The E_{HOMO}, E_{LUMO} and energy gap of the intermediates during the photocatalytic degradation of MO were calculated to clarify the structure and evolution of these intermediates. The results are shown in Fig. 11 and Table 1. The E_{HOMO} of MO~P13 are -7.70277 eV, -7.14816 eV, -7.51182 eV, -8.45077 eV, -7.80096 eV, -7.94131 eV, -7.75934 eV, -7.85046 eV, -9.64866 eV, -7.76587 eV, -7.23846 eV, 7.36413 eV, -8.52829 eV, -7.51482 eV. The E_{HOMO} of MO~P13 are 1.14403 eV, 2.19450 eV, 2.97133 eV, 1.69347 eV, 1.14267 eV, 1.12907 eV, 1.29554 eV, 1.28955 eV, 1.48458 eV, 2.98792 eV, 3.00478 eV, 3.00587 eV, 2.84702 eV, 4.31419 eV. The energy gap of MO~P13 are 8.8468 eV, 9.34266 eV, 10.48315 eV, 10.14424 eV, 8.94363 eV, 9.07038 eV, 9.05488 eV, 9.14002 eV, 11.13323 eV, 10.75379 eV, 10.24325 eV, 10.37 eV, 11.37531 eV, 11.82901 eV. The energy gap of MO~P13 shows a gradual upward trend. The energy gap value of MO was 8.8468 eV, and those of P1~P13 ranged from 9.34266 eV to 11.82901 eV, with the energy gap of MO being the smallest. The chemical hardness also shows a gradual upward trend. The chemical hardness of MO is 4.4234 eV, and the chemical hardness values of P1~P13 were between 4.67133 eV and 5.9145 eV, with the chemical hardness of MO being the lowest. The chemical softness shows a gradual downward trend. The chemical softness value of MO is 0.11304 eV, and the chemical softness values of P1-P13 were between 0.10704 eV and 0.08454 eV, with the chemical softness of MO being the highest.[39,40]

The possible degradation pathways of *p*-NP are shown in Fig. 12. The first path is the reduction of *p*-NP to produce *p*-aminophenol (*p*-NP-P1),[41] followed by catalytic hydrolysis to yield hydroquinone (*p*-NP-P2), and then oxidation to produce 1,2,4-trihydroxybenzene (*p*-NP-P3). The second pathway may also be the reduction reaction of *p*-NP to *p*-nitrosophenol (*p*-NP-P4). After this reduction reaction, *p*-aminophenol (*p*-NP-P1) is generated.[42] Subsequently, after catalytic hydrolysis or deamination, hydroquinone (*p*-NP-P2) or phenol (*p*-NP-P5) is formed. Moreover, p-NP-P5 can be hydroxylated by hydrogen peroxide to produce *p*-NP-P2 and 1,2-dihydroxybenzene (*p*-NP-P7).[43] The third pathway may involve *p*-NP undergoing hydrogen oxidation or denitrification to generate *p*-NP-P5 or 2,4-dinitrophenol (*p*-NP-P6). Subsequently, *p*-NP-P6 undergoes denitrification to form 1,2-dihydroxybenzene (*p*-NP-P7).

The Developmental toxicity, Mutagenicity, Bioaccumulation factor and Rat oral toxicity LD_{50} ($mg \cdot kg^{-1}$) of *p*-NP and *p*-NP-DPs (P1, P2, P3, P4, P5, P6, P7) during the treatment of ZnO/MXene composite materials were evaluated by T.E.S.T. calculation, and a series of *p*-NP-DPs intermediates were selected. To evaluate the biotoxicity of ZnO/MXene composites treated by degradation process. *p*-NP and *p*-NP-DPs exhibited a "Developmental toxicant" phenotype, whereas ZnO/MXene composite treatment increased the Developmental toxicity of P1, P2, P3, P4, P5, P6, and P7 (Fig. 13a and Table S12). *p*-NP and *p*-NP-DPs exhibited a "Mutagenicity positive" state, whereas the ZnO/MXene composite treatment reduced the Mutagenicity of P2, P3, P4, and P5 and increased the Mutagenicity of P1, P6,

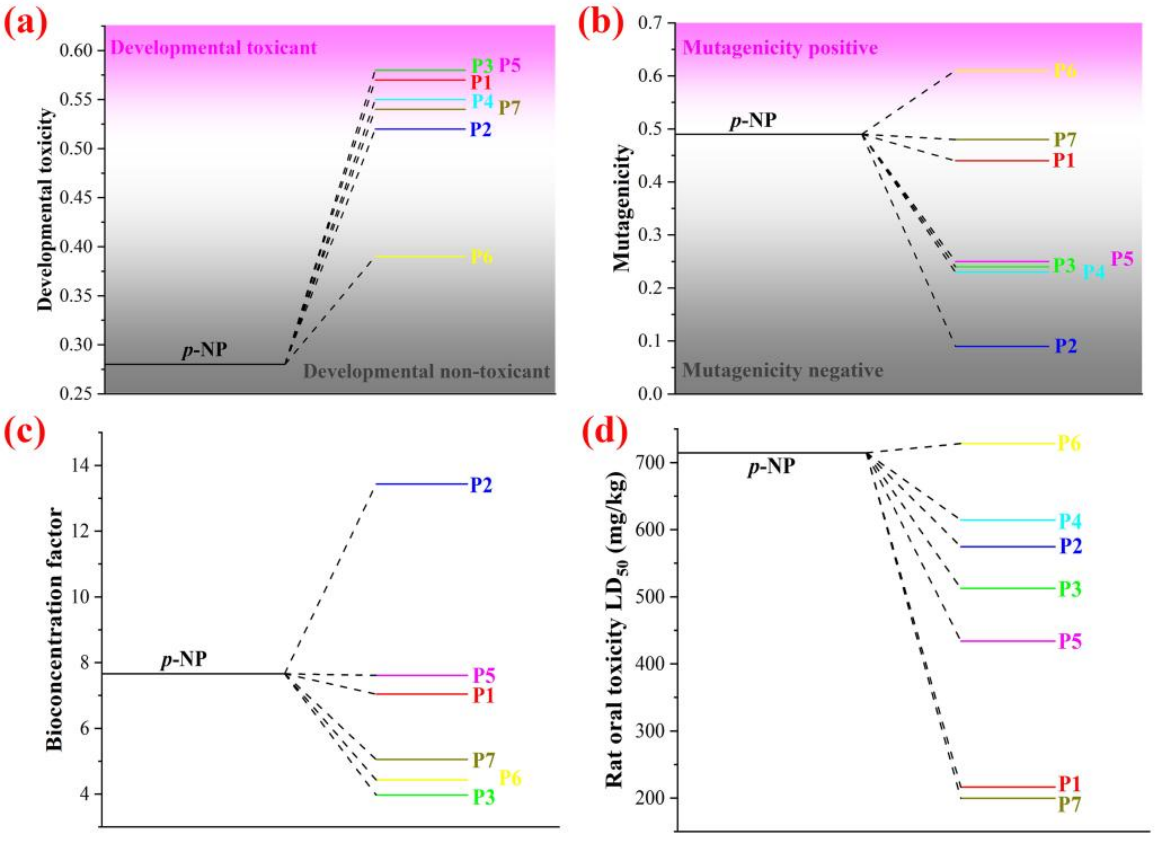

Fig. 13: Developmental toxicity (a), Mutagenicity (b), Bioaccumulation factor (c), Rat oral toxicity LD_{50} ($mg \cdot kg^{-1}$) (d) for *p*-NP and *p*-NP-DPs.

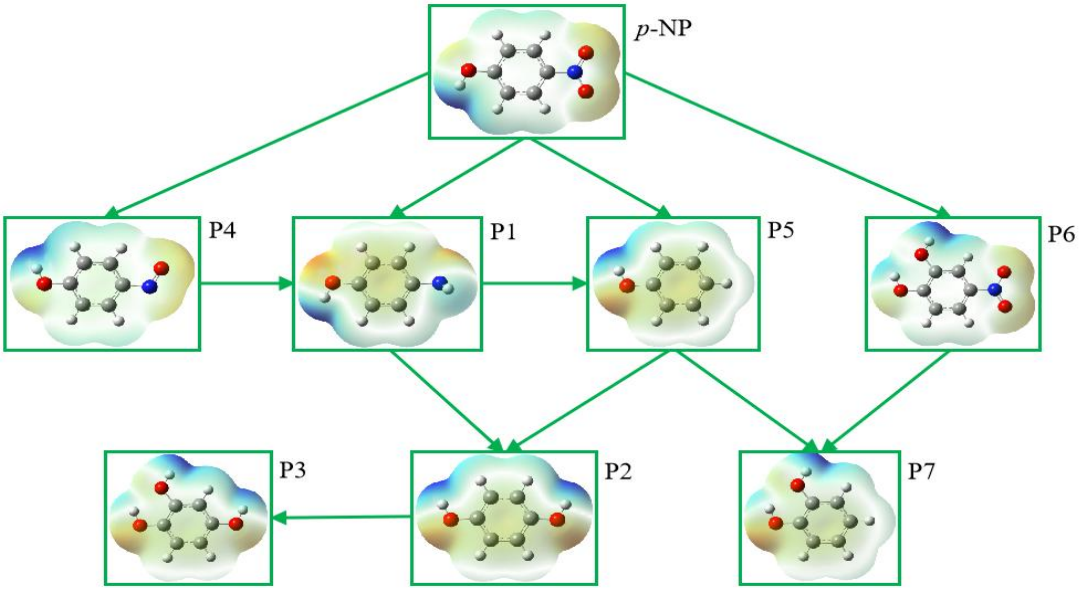

Fig. 14: Bulk electrostatic potential of *p*-NP.

and P7 (Fig. 13b and Table S12). The ZnO/MXene composite process reduced the Bioaccumulation factor of P1, P3, P5, P6, P7, and P8 and increased the Bioaccumulation factor of P2 (Fig. 13c and Table S12). ZnO/MXene composite treatment reduced Rat oral toxicity LD_{50} ($mg \cdot kg^{-1}$) in P1, P2, P3, P4, P5, P7, P8 rats and increased Rat oral toxicity LD_{50} ($mg \cdot kg^{-1}$) in P6 rats (Fig. 13d and Table S12).

The charge distribution can be described by ESP, and the results of ESP of *p*-NP are shown in Figs. 14-15. The presence of red and blue regions can assist us in understanding the charge distribution of molecules in different areas. The charge distribution is crucial for comprehending the position of the bulk phase charge distribution, as well as the reactivity and the mechanisms of electrophilic and nucleophilic reactions. For *p*-

NP, *p*-NP-P4, and *p*-NP-P6, the red region on the right side of the ESP indicates the N=O bond, the blue region represents the O-H bond. For *p*-NP, *p*-NP-P1, *p*-NP-P2, *p*-NP-P3, *p*-NP-P4, *p*-NP-P5, *p*-NP-P6, and *p*-NP-P7, the red region on the left side of the ESP corresponds to the C-O bond. The difference in the surface charge distribution mainly stems from the structural and length differences of the N=O bonds, O-H bonds, C-O bonds, and hydrocarbon chains. The regions enriched with negative charges are precisely the red regions.

The E_{HOMO}, E_{LUMO} and energy gap of the intermediates during the photocatalytic degradation of *p*-NP were calculated to clarify the structure and evolution of the intermediates during the photocatalytic degradation of *p*-NP. The results are shown in Fig. 16 and Table 2. The E_{HOMO} of *p*-NP~P7 are -0.35853 eV, -0.31185 eV, -0.30032 eV, -0.29399 eV, -0.34146 eV, -0.31722 eV, -0.34558 eV, -0.30757 eV. The E_{LUMO} of *p*-

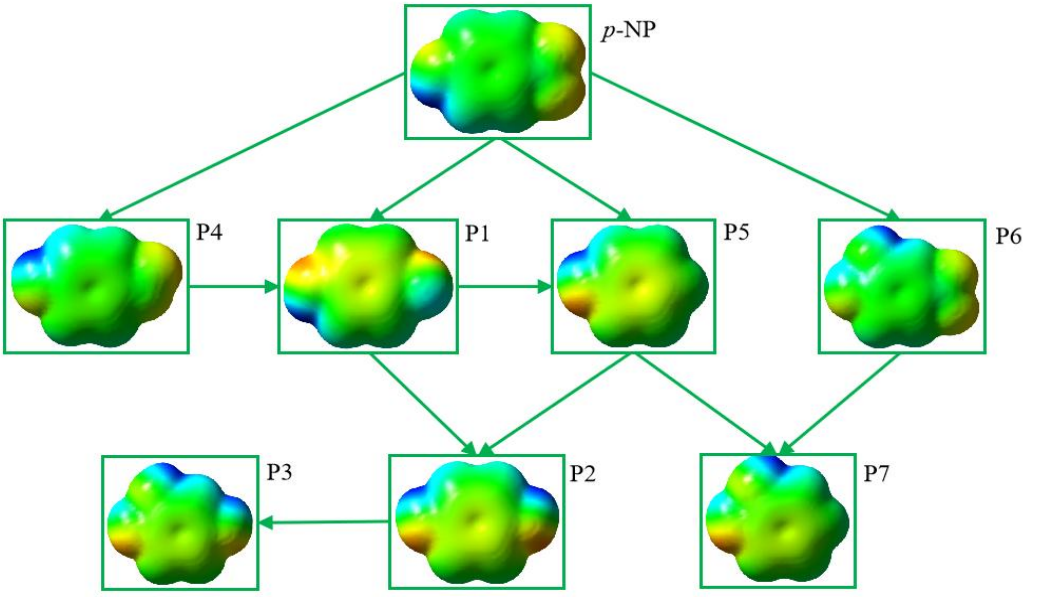

Fig. 15: Surface electrostatic potential of *p*-NP.

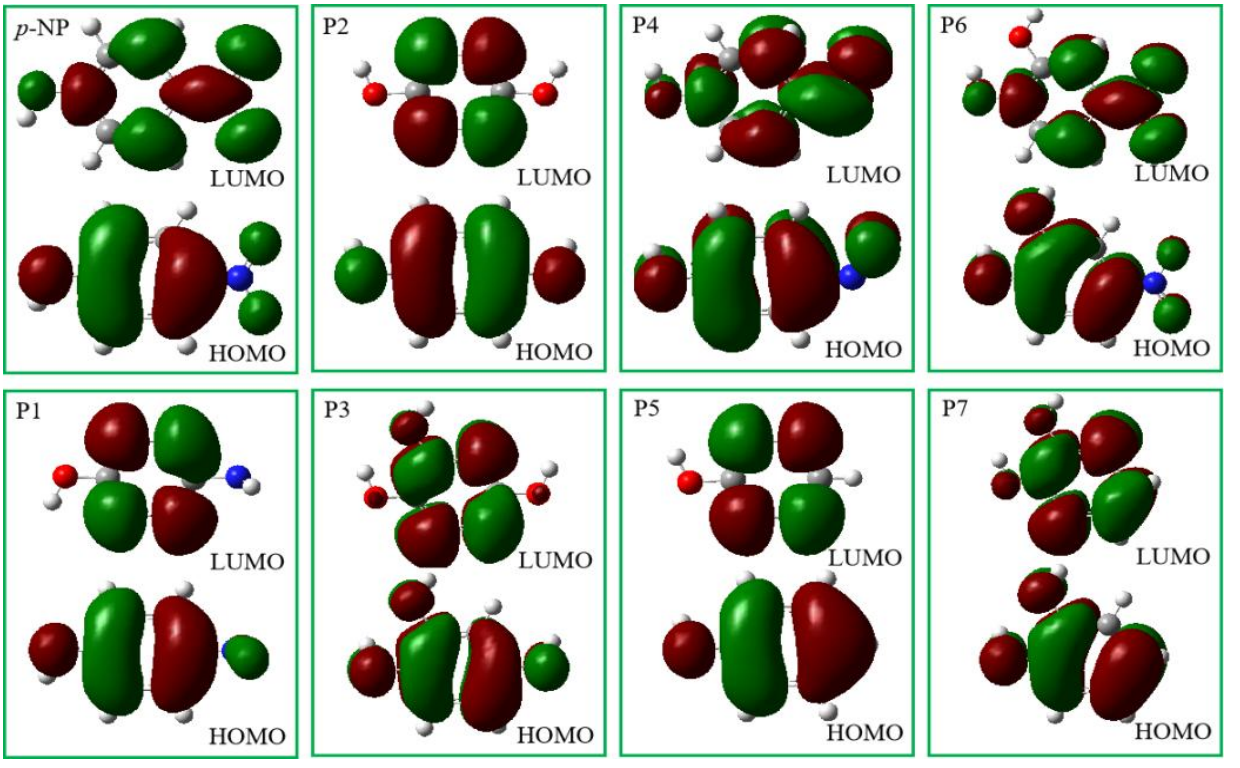

Fig. 16: The changes of E_{HOMO} and E_{LUMO} of *p*-NP.

NP~P7 are 0.04787 eV, 0.14595 eV, 0.13737 eV, 0.14393 eV, 0.06226 eV, 0.14492 eV, 0.04312 eV, 0.14934 eV. The energy gap of *p*-NP~P7 are 0.40640 eV, 0.45780 eV, 0.43769 eV, 0.43792 eV, 0.40372 eV, 0.46214 eV, 0.38870 eV, 0.45691 eV. The E_{HOMO}, ionization potential, electronegativity, chemical potential and electrophilicity index were studied, and five rules were found. The E_{HOMO} of *p*-NP~P7 shows a gradual upward trend. The E_{HOMO} value of *p*-NP was-0.35853 eV, and the E_{HOMO} values of P1~P7 were -0.31185 eV, -0.30757 eV, and the E_{HOMO} value of *p*-NP was the largest. The ionization potential shows a gradual downward trend. The lonization potential of *p*-NP is 0.35853 eV, The ionization potential

Table 2: The law of the parameters of the *p*-NP orbit.

Name	E_{HOMO}	E_{LUMO}	Energy gap (E_{HOMO}-E_{LUMO})	Ionization potential (I=-E_{HOMO})	Electron affinity (A=-E_{LUMO})	Electron affinity (η=(I-A)/2)	Chemical softness (ζ=1/2η)	Electronegativity (X=(I+A)/2)	Chemical potential (μ=-(I+A)/2)	Electrophilicity index (ω=μ²/2η)
p-NP	-0.36	0.05	0.41	0.36	-0.05	0.20	2.46	0.16	-0.16	0.06
P1	-0.31	0.15	0.46	0.31	-0.15	0.23	2.18	0.08	-0.08	0.02
P2	-0.30	0.14	0.44	0.30	-0.14	0.22	2.28	0.08	-0.08	0.02
P3	-0.29	0.14	0.44	0.29	-0.14	0.22	2.28	0.08	-0.08	0.01
P4	-0.34	0.06	0.40	0.34	-0.06	0.20	2.48	0.14	-0.14	0.05
P5	-0.32	0.14	0.46	0.32	-0.14	0.23	2.16	0.09	-0.09	0.02
P6	-0.35	0.04	0.39	0.35	-0.04	0.19	2.57	0.15	-0.15	0.06
P7	-0.31	0.15	0.46	0.31	-0.15	0.23	2.19	0.08	-0.08	0.01

Table 3: Literature summary on the photocatalytic degradation and removal of organic pollutants.

Advanced oxidation technology	Catalyst	Pollutant	Pollutant concentration	Dosage of catalyst	Removal rate	References
Photocatalysis technology	ZnO/MXene	MO *p*-NP	20 mg·L^{-1}	0.5 g·L^{-1} 0.7 g·L^{-1}	MO:100% *p*-NP:74% (180 min)	This work
	MXene-MOFs (MCoO@Co-N-C)	BPA	20 mg·L^{-1}	5 mg	100% (10min)	[27]
	$BiOBr/Bi_2MoO_6$@MXene	CR, TC, CIP	CR：100 ppm TC：20 ppm CIP：20 ppm	-	CR: 98.89% TC: 92.1% CIP: 90%	[13]
	$ZnO/Ti_3C_2T_x$	MO, RhB	-	30 mg	MO: 99.7% (50 min) RhB: 99.8% (70 min)	[48]
	ZnO/MXene	RhB	10^{-5}mol·L^{-1}	100 mg	RhB: 97.5% (18 min)	[6]
	$SrTiO_3/Ti_3C_2T_x$(ST-10)	TC	10 mg·L^{-1}	-	100% (10 min)	[49]
	ZnO@C07	MB	10 mg·L^{-1}	20 mg	95.6% (900 min)	[50]
Fenton-like technology	MXene/Fe-Al LDH	TC	20 mg·L^{-1}	100 mg	80 %	[51]

values of P1-P7 were between 0.31185 eV and 0.30757 eV, and the ionization potential value of *p*-NP was the lowest. The electronegativity shows a gradual downward trend. The electronegativity value of *p*-NP is0.15533 eV, the electronegativity values of P1-P7 were between 0.07912 eV and 0.15123 eV, and the electronegativity value of *p*-NP was the lowest. The chemical potential shows a gradual upward trend. The chemical potential value of *p*-NP is -0.15533 eV, The chemical potential values of P1~P7 were between -0.15123 eV and -0.07503 eV, and the chemical potential value of *p*-NP was the largest. The electrophilicity index shows a gradual downward trend. The electrophilicity index value of *p*-NP is0.05937 eV, the electrophilicity index values of P1~P7 were between 0.01286 eV and 0.05884 eV, and the electrophilicity index value of *p*-NP was the lowest.[44,45]

3.5 Environmental implication

In this paper, 0D/2D ZnO/MXene photocatalysts with synergistically enhanced photocatalytic performance were constructed. By leveraging the interface effect between MXene and ZnO, along with the nanoconfinement effect of 2D MXene, ZnO/MXene materials exhibit outstanding photocatalytic activity. 0D ZnO nanoparticles are embedded on the surface of 2D MXene to construct a 0D/2D heterostructure with an effective contact interface. This heterostructure can promote the separation and transfer of photogenerated charges.[46] The d-orbital electrons of ZnO can be excited to the conduction band and interact with the p-orbital electrons of organic pollutants, leading to the formation of new chemical bonds or the breaking of original chemical bonds. By integrating the orbital changes during the degradation process of organic pollutants in water treatment, the 0D/2D photocatalytic model can significantly enhance the photocatalytic efficiency and selectivity, which provided an effective strategy for the removal of environmental pollutants.[47]

In Table 3, the degradation performance of ZnO/MXene photocatalyst was compared with reported references. Here, different catalysts used in various advanced oxidation techniques are compared, and it is clear that ZnO/MXene photocatalyst exhibits better photocatalytic performance, achieving 100% removal of MO after an 180 minutes reaction. Therefore, by leveraging the nanoconfinement effect of 2D MXene and the interface effect between MXene and the metal oxide, efficient separation of photogenerated hole - electron pairs is achieved. The nanoconfinement space constructed by the interface of MXene layers leads to the enrichment of radical/nonradica, ultimately realizing the efficient and rapid photocatalytic degradation of organic pollutants. This study provides theoretical and data support for enriching and improving the related mechanisms of confined catalysis, and provides support for the construction of efficient photocatalytic systems and the synergy between sewage treatment and carbon reduction.

4. Conclusion

The polymeric spherical ZnO nanoparticles could be clearly observed on the surface layer, edges, and inter-layer gaps of the layered MXene structure, forming a composite photocatalyst with a sandwich-like structure. The presence of MXene enhanced the response to visible light. When the mass ratio of ZnO to MXene in the ZnO/MXene composite was 1:1, and the catalyst dosages were 0.5 $g \cdot L^{-1}$ and 0.7 $g \cdot L^{-1}$ respectively, the photocatalytic activity of the ZnO/MXene composite was evaluated. The optimal removal rates of MO and *p*-NP were 100% and 74% respectively. The mechanisms for the enhancement of photocatalytic activity included the nanoconfinement effect of MXene and the interface effect between ZnO and MXene. The photocatalytic degradation processes of MO and *p*-NP were different. The difference in the surface charge distribution of MO mainly originated from the S=O bond. The energy gap and chemical hardness of MO-DPs showed an upward trend. In contrast, the difference in the surface charge distribution of *p*-NP mainly stemmed from the N=O bond. The E_{HOMO} value and chemical potential value of *p*-NP-DPs showed an upward trend, while the electronegativity value and electrophilicity index showed a downward trend. The toxicity test showed that the intermediates in the photocatalytic degradation processes of MO and *p*-NP had the potential for increased toxicity.

Acknowledgement

This study is supported by the China National University Student Innovation & Entrepreneurship Development Program (202410429017), National Natural Science Foundation of China (41672340), Taishan Scholar Foundation of Shandong Province (tsqn201909126), National Key Research and Development Program of China (2021YFC3201004), Natural Science Foundation of Shandong Province (ZR2020QE230, ZR2021QE087, ZR2024QB324), and Qingdao Postdoctoral Application Research Project (QDBSH20240202130).

Conflict of Interest

There is no conflict of interest.

Supporting Information

Applicable.

References

[1] A. Fujishima, K. Honda, Electrochemical photolysis of water at a semiconductor electrode, *Nature*, 1972, **238**, 37-38, doi: 10.1038/238037a0.

[2] A. R. Bhapkar, S. Bhame, A review on ZnO and its modifications for photocatalytic degradation of prominent textile effluents: Synthesis, mechanisms, and future directions, *Journal of Environmental Chemical Engineering*, 2024, **12**, 112553, doi: 10.1016/j.jece.2024.112553.

[3] P. Dhiman, G. Rana, A. Kumar, G. Sharma, D. V. N. Vo, M.

Naushad, ZnO-based heterostructures as photocatalysts for hydrogen generation and depollution: A review, *Environmental Chemistry Letters*, 2022, **20**, 1047-1081, doi: 10.1007/s10311-021-01361-1.

[4] F. H. Abdullah, N. H. H. A. Bakar, M. A. Bakar, Current advancements on the fabrication, modification, and industrial application of zinc oxide as photocatalyst in the removal of organic and inorganic contaminants in aquatic systems, *Journal of Hazardous Materials Advances*, 2022, **424**, 127416, doi: 10.1016/j.jhazmat.2021.127416.

[5] W. L. Yu, J. F. Zhang, T. Y. Peng, New insight into the enhanced photocatalytic activity of N-, C-and S-doped ZnO photocatalysts, *Applied Catalysis B: Environmental*, 2016, **181**, 220-227, doi: 10.1016/j.apcatb.2015.07.031.

[6] M. F. Khadidja, J. C. Fan, S. Y. Li, S. D. Li, K. X. Cui, J. H. Wu, W. G. Zeng, H. G. Wei, H. G. Jin, N. Naik, Z. S. Chao, D. Pan, Z. H. Guo, Hierarchical ZnO/MXene composites and their photocatalytic performances, *Colloids and Surfaces a-Physicochemical and Engineering Aspects*, 2021, **628**, 127230, doi: 10.1016/j.colsurfa.2021.127230.

[7] S. L. Li, Y. L. Li, Z. Y. Yuan, J. Z. Li, D. Butenko, Y. J, I. Shanenkov, G. S Li, W. Han, A novel MXene-bridged Z-scheme ZnO@Nb_2CT_x MXene@carbon nitride nanosheets photocatalyst for efficient enrofloxacin degradation, *Chemical Engineering Journal*, 2024, **489**, 151505, doi: 10.1016/j.cej.2024.151505.

[8] H. H. Gong, F. Wang, Q. Li, L. X. Wei, J. Zhang, Y. Ma, Y. F. Rui, X. L. Shi, Selective hydrogenative rearrangement of furfural to cyclopentanol over alloyed Cu-Co supported on sulfur-doped coffee biochar, *ACS Sustainable Chemistry & Engineering*, 2024, **12**, 7211-7225, doi: 10.1021/acssuschemeng.4c02304.

[9] H. H. Gong, L. X. Wei, Q. Li, J. Zhang, F. Wang, J. Ren, X. L. Shi, Electron-rich Ru supported on N-Doped coffee biochar for selective reductive amination of furfural to furfurylamine, *Langmuir*, 2024, **40**, 8950-8960, doi: 10.1021/acs.langmuir.4c00112.

[10] Z. Liu, X. Y. Xu, F. Xu, R. D. Su, B. Li, F. Zhang, X. Xu, Y. Wang, D. F. Ma, B. Y. Gao, Q. Li, Diatomic "catalytic/co-catalytic" Fe/Mo catalysts promote Fenton-like reaction to treat organic wastewater through special interfacial reaction enhancement mechanism, *Water Research*, 2025, **274**, 123147, doi: 10.1016/j.watres.2025.123147.

[11] Y. A. Hao, F. Hu, S. Q. Zhu, Y. J. Sun, H. Wang, L. Q. Wang, Y. Wang, J. J. Xue, Y. F. Liao, M. H. Shao, S. J. Peng, MXene-regulated metal-oxide interfaces with modified intermediate configurations realizing nearly 100% CO_2 electrocatalytic conversion, *Angewandte Chemie-International Edition*, 2023, **62**, e202304179, doi: 10.1002/anie.202304179.

[12] Y. Wang, C. X. Yang, Y. L. Liu, Y. Q. Fan, F. Dang, Y. Qiu, H. M. Zhou, W. L. Wang, Y. Z. Liu, Solvothermal synthesis of ZnO nanoparticles for photocatalytic degradation of methyl orange and *p*-nitrophenol, *Water*, 2021, **13**, 3224, doi: 10.3390/w13223224.

[13] Z. M. Yang, Q. Q. Lin, G. Y. Zeng, S. M. Zhao, G. L. Yan, M. B. M. Y. Ang, Y. H. Chiao, S. Y. Pu, Ternary hetero-structured BiOBr/Bi_2MoO_6@ MXene composite membrane: Construction and enhanced removal of antibiotics and dyes from water, *Journal of Membrane Science*, 2023, **669**, 121329, doi: 10.3390/w13223224.

[14] A. F. Du, H. F. Fu, P. Wang, C. Zhao, C. C. Wang, Enhanced catalytic peroxymonosulfate activation for sulfonamide antibiotics degradation over the supported CoS_x-CuS_x derived from ZIF-L(Co) immobilized on copper foam, *Journal of Hazardous Materials Letters*, 2022, **426**, 128134, doi: 10.1016/j.jhazmat.2021.128134.

[15] C. X. Yang, X. N. Wang, X. Y. Zhao, Y. K. Wu, J. Y. Lin, Y. H. Zhao, Y. Y. Xu, K. P. Sun, C. Zhang, Z. H. Wan, W. H. Zhao, H. F. Sun, D. Chen, W. P. Dong, T. Y. Wang, W. L. Wang, Effect of fluorine atoms and piperazine rings on biotoxicity of norfloxacin analogues: Combined experimental and theoretical study, *Environment & Health*, 2024, **2**, 886-901, doi: 10.1021/envhealth.4c00095.

[16] J. Zhang, T. Lu, Efficient evaluation of electrostatic potential with computerized optimized code, *Chemical Physics*, 2021, **23**, 20323-20328, doi: 10.1039/D1CP02805G.

[17] D. Sharma, S. N. Tiwari, Electronic structure and vibrational spectra of 1OCB liquid crystal: A DFT study, *Emerging Materials Research*, 2017, **6**, 322-330, doi: 10.1680/jemmr.15.00052.

[18] C. X. Yang, Z. H. Wan, H. C. Wang, J. Q. Zang, X. N. Wang, F. Yang, G. D. Zhang, W. H. Zhao, L. Liu, Y. L. Liu, W. P. Dong, W. J. Xie, Y. Z. Tang, W. L. Wang, Temperature-dependent adsorption process of neonicotinoid insecticide nitenpyram by sawdust biochar: Mechanism and theoretical simulation, *ACS Agricultural Science & Technology*, 2023, **4**, 22-33, doi: 10.1021/acsagscitech.3c00228.

[19] A. Saeed, M. Altarawneh, K. Siddique, J. A. Conesa, N. Ortuño, B. Z. Dlugogorski, Photodecomposition properties of brominated flame retardants (BFRs), *Ecotoxicology and Environmental Safety*, 2020, **192,** 110272, doi: 10.1016/j.ecoenv.2020.110272.

[20] A. Sengupta, B. Li, D. Svatunek, F. Liu, K. N. Houk, Cycloaddition reactivities analyzed by energy decomposition analyses and the frontier molecular orbital model, *Accounts of Chemical Research*, 2022, **55**, 2467-2479, doi: 10.1021/acs.accounts.2c00343.

[21] M. B. Feng, R. J. Qu, C. Wang, L. S. Wang, Z. Y. Wang, Comparative antioxidant status in freshwater fish Carassius auratus exposed to six current-use brominated flame retardants: A combined experimental and theoretical study, *Aquatic Toxicology*, 2013, **140,** 314-323, doi: 10.1016/j.aquatox.2013.07.001.

[22] J. J. Gu, X. C. Lu, G. J. Li, B. L. Shan, J. H. Liu, Y. X. Qu, H. Ye, K. Xi, H. H. Wu, Beyond carbon dots: Intrinsic reducibility in Ti_3C_2 MXene quantum dots induces ultrasensitive fluorescence detection and scavenging of Mn(VII), *Chemical Engineering Journal*, 2023, **467**, 143445, doi: 10.1016/j.cej.2023.143445.

[23] L. Yuan, J. B. Cai, J. C. Xu, Z. H. Yang, H. H. Liang, Q. S. Su, J. L. Wang, In situ growth of ZnO nanosheets on $Ti_3C_2T_x$ MXene for superior-performance zinc-nickel secondary battery, *Chemical Engineering Journal*, 2023, **451**, 139073, doi:

10.1016/j.cej.2022.139073.
[24] M. Afsharpour, L. Radmanesh, C. X. Yang, In situ synthesis of doped bio-graphenes as effective metal-free catalysts in removal of antibiotics: Effect of natural precursor on doping, morphology, and catalytic activity, *Molecules*, 2023, **28**, 7212, doi: 10.3390/molecules28207212.
[25] X. Zhao, H. Xu, Z. Y. Hui, Y. Sun, C. Y. Yu, J.L. Xue, R. C. Zhou, L. M. Wang, H. H. Dai, Y. Zhao, J. Yang, J. Y. Zhou, Q. Chen, G. Z. Sun, W. Huang, Electrostatically assembling 2D nanosheets of MXene and MOF-derivatives into 3D hollow frameworks for enhanced lithium storage, *Small*, 2019, **15**, 1904255, doi: 10.1002/smll.201904255.
[26] M. Naguib, O. Mashtalir, M. R. Lukatskaya, B. Dyatkin, C. F. Zhang, V. Presser, Y. Gogotsi, M. W. Barsoum, One-step synthesis of nanocrystalline transition metal oxides on thin sheets of disordered graphitic carbon by oxidation of MXenes, *Chemical Communications*, 2014, **50**, 7420-7423, doi: 10.1039/C4CC01646G.
[27] X. Guo, H. Zhang, Y. Y. Yao, C. M. Xiao, X. Yan, K. Chen, J. W. Qi, Y. .J. Zhou, Z. G. Zhu, X. Y. Sun, J. S. Li, Derivatives of two-dimensional MXene-MOFs heterostructure for boosting peroxymonosulfate activation: Enhanced performance and synergistic mechanism, *Applied Catalysis B: Environmental*, 2023, **323**, 122136, doi: 10.1016/j.apcatb.2022.122136.
[28] H. X. Shi, J. Y. Chen, G. Y. Li, X. Nie, H. J. Zhao, P. K. Wong, T. C. An, Synthesis and characterization of novel plasmonic Ag/AgX-CNTs (X = Cl, Br, I) nanocomposite photocatalysts and synergetic degradation of organic pollutant under visible light, *ACS Applied Materials & Interfaces*, 2013, **5**, 6959-6967, doi: 10.1021/am401459c.
[29] B. Saini, H. K, D. Laishram, R. Krishnapriya, R. Singhal, R. K. Sharma, Role of ZnO in ZnO nanoflake/Ti_3C_2 MXene composites in photocatalytic and electrocatalytic hydrogen evolution, *ACS Applied Nano Materials*, 2022, **5**, 9319-9333, doi: 10.1021/acsanm.2c01639.
[30] T. Torchynska, B. E. I. Filali, J. A. J. Gomez, G. Poloupan, J. L. R. García, L. Shcherbyna, Raman scattering, emission, and deep defect evolution in ZnO: In thin films, *Journal of Vacuum Science & Technology A*, 2020, **38**, 063409, doi: 10.1116/6.0000364.
[31] W. Q. Liu, M. Zhou, H. Q. Fu, Design of Ag@ZnO@Ti_3C_2 MXene heterojunction photocatalyst for enhanced photocatalytic degradation activity of methylene blue and levofloxacin under visible light irradiation, *Journal of Environmental Chemical Engineering*, 2023, **11**, 110926, doi: 10.1016/j.jece.2023.110926.
[32] Y. Lu, Y. Zhang, J. Zhang, Z. Li, F. Hu, D. Pan, S. Melhi, X. Shi, M. A. Amin, Z. M. El-Bahy, Q. Shao, Electrochemically synthesized Tin micro-nanometer powders for visible light photocatalytic degradation of Rhodamine B dye from polluted water, *Advanced Composites and Hybrid Materials*, 2024, **7**, 110, doi: 10.1007/s42114-024-00921-7.
[33] Y. Qiu, C. X. Yang, H. M. Zhou, J. Q. Zang, Y. Q. Fan, F. Dang, G. W. Cui, W. L. Wang, Enriched surface oxygen vacancies of $Fe_2(MoO_4)_3$ catalysts for a PDS-activated photoFenton system, *Molecules*, 2022, **28**, 333, doi: 10.3390/molecules28010333.
[34] H. M. Zhou, Y. Qiu, C. X. Yang, J. Q. Zang, Z. H. Song, T. Z. Yang, J. Z. Li, Y. Q. Fan, F. Dang, W. L. Wang, Efficient degradation of congo red in water by UV-vis driven $CoMoO_4$/PDS photo-fenton system, *Molecules*, 2022, **27**, 8642, doi: 10.3390/molecules27248642.
[35] C. H. Nguyen, C. C. Fu, R. S. Juang, Degradation of methylene blue and methyl orange by palladium-doped TiO_2 photocatalysis for water reuse: Efficiency and degradation pathways, *Journal of Cleaner Production*, 2018, **202**, 413-427, doi: 10.1016/j.jclepro.2018.08.110.
[36] T. Zhang, C. S. Dong, L. Z. Zhang, Solar-assisted-self-healing N-doped MXene quantum dots-based membrane with protein resistance for seawater desalination, *Environmental Science & Technology*, 2023, **57**, 9996-10007, doi: 10.1021/acs.est.3c03013.
[37] S. Jangra, A. Raza, B. Kumar, J. Sharma, S. Das, K. Pandey, Y. K. Mishra, M. S. Goyat, MXene decorated ZnO-tetrapod for efficient degradation of Methyl Orange, Methylene Blue, and Rhodamine B dyes, *Materials Science and Engineering B-Advanced Functional Solid-State Materials*, 2025, **311**, 117832, doi: 10.1016/j.mseb.2024.117832.
[38] R. L. Yin, Y. X. Chen, S. X. He, W. B. Li, L. X. Zeng, W. Q. Guo, M. S. Zhu, In situ photoreduction of structural Fe(III) in a metal-organic framework for peroxydisulfate activation and efficient removal of antibiotics in real wastewater, *Journal of Hazardous Materials*, 2020, **388**, 121996, doi: 10.1016/j.jhazmat.2019.121996.
[39] U. Habiba, S. Mutahir, M. A. Khan, M. Humayun, M. S. Refat, K. S. Munawar, Effective removal of refractory pollutants through cinnamic acid-modified wheat husk biochar: Experimental and DFT-based analysis, *Catalysts*, 2022, **12**, 1063, doi: 10.3390/catal12091063.
[40] P. Kimber, F. Plasser, Energy component analysis for electronically excited states of molecules: Why the lowest excited state is not always the HOMO/LUMO transition, *Journal of Chemical Theory and Computation*, 2023, **19**, 2340-2352, doi: 10.1021/acs.jctc.3c00125.
[41] G. Yadav, M. Ahmaruzzaman, New generation advanced nanomaterials for photocatalytic abatement of phenolic compounds, *Chemosphere*, 2022, **304**, 135297, doi: 10.1016/j.chemosphere.2022.135297.
[42] J. Li, Y. Ren, F. Z. Ji, B. Lai, Heterogeneous catalytic oxidation for the degradation of *p*-nitrophenol in aqueous solution by persulfate activated with $CuFe_2O_4$ magnetic nano-particles, *Chemical Engineering Journal*, 2017, **324**, 63-73, doi: 10.1016/j.cej.2017.04.104.
[43] J. Yang, B. Pan, H. Li, S. H. Liao, D. Zhang, M. Wu, B. S. Xing, Degradation of *p*-nitrophenol on biochars: Role of persistent free radicals, *Environmental Science & Technology*, 2016, **50**, 694-700, doi: 10.1021/acs.est.5b04042.
[44] R. Casares, Á. M. Pinel, S. R. González, I. R. Márquez, L. Lezama, M. T. González, E. Leary, V. Blanco, J. G. Fallaque, C. Díaz, F. Martín, J. M. Cuerva, A. Millán, Engineering the HOMO-LUMO gap of indeno [1,2-*b*] fluorene, *Journal of Materials Chemistry C*, 2022, **10**, 11775-11782, doi:

10.1039/d2tc02475f.
[45] B. Mazouin, A. A. Schöpfer, O. A. V. Lilienfeld, Selected machine learning of HOMO-LUMO gaps with improved data-efficiency, *Materials Advances*, 2022, **3**, 8306-8316, doi: 10.1039/d2ma00742h.
[46] S. A. Mahadik, A. Patil, H. M. Pathan, S. Salunke-Gawali, R. J. Butcher, Thionaphthoquinones as photosensitizers for TiO_2 nanorods and ZnO nanograin based dye-sensitized solar cells: Effect of nanostructures on charge transport and photovoltaic performance, *Engineered Science*, 2020, **14**, 46-58, doi: 10.30919/es8d1160.
[47] P. Vairale, V. Sharma, B. Bade, A.Waghmare, P. Shinde, A. Punde, V. Doiphode, R. Aher, S. Pandharkar, S. Nair, V. Jadkar, P. Shelke, M.Prasad, S. Jadkar, Melanin sensitized nanostructured ZnO photoanodes for efficient photoelectrochemical splitting of water: Synthesis and characterization, *Engineered Science*, 2020, **11**, 76-84, doi: 10.30919/es8d0023.
[48] Q. T. H. Ta, N. M. Tran, J. S. Noh, Rice crust-like ZnO/$Ti_3C_2T_x$ MXene hybrid structures for improved photocatalytic activity, *Catalysts*, 2020, **10**, 1140, doi: 10.3390/catal10101140.
[49] X. W. Wu, J. Chen, X. F. Yang, H. Q. Zheng, Y. Z. Ma, Y. J. Li, Synergistic activation of peroxymonosulfate for tetracycline hydrochloride degradation with $SrTiO_3$/$Ti_3C_2T_x$ photocatalyst, *Applied Surface Science*, 2025, **680**, 161317, doi: 10.1016/j.apsusc.2024.161317.
[50] C. X. Yang, X. N. Wang, Y. J. Ji, T. Ma, F. Zhang, Y. Q. Wang, M. W. Ci, D.T. Chen, A. X. Jiang, W. L. Wang, Photocatalytic degradation of methylene blue with ZnO@C nanocomposites: Kinetics, mechanism, and the inhibition effect on monoamine oxidase A and B, *Nanoimpact*, 2019, **15**, 100174, doi: 10.1016/j.impact.2019.100174.
[51] Z. Z. Yang, Z. Y. Zhou, X. F. Tan, G. M. Zeng, C. Zhang, MXene-induced electronic structure modulation of Fe-Al-LDH to boost the Fenton-like Reaction: Singlet oxygen evolution and electron-transfer mechanisms, *Journal of Materials Science & Technology*, 2025, **204,** 224-237, doi: 10.1016/j.jmst.2024.03.023.